

The evolution of the dust-to-metals ratio in high-redshift galaxies probed by GRB-DLAs[★]

P. Wiseman¹, P. Schady¹, J. Bolmer¹, T. Krühler¹, R. M. Yates¹, J. Greiner¹, and J. P. U. Fynbo²

¹ Max-Planck-Institute für Extraterrestrische Physik (MPE), Giessenbachstrasse 1, 85748 Garching, Germany
e-mail: wiseman@mpe.mpg.de

² Dark Cosmology Centre, Niels Bohr Institute, University of Copenhagen, Juliane Maries Vej 30, 2100 Copenhagen, Denmark

received date/accepted date

ABSTRACT

Context. Several issues regarding the nature of dust at high redshift remain unresolved: its composition, its production and growth mechanisms, and its effect on background sources.

Aims. This paper aims to provide a more accurate relation between dust depletion levels and dust-to-metals ratio (DTM), and to use the DTM to investigate the origin and evolution of dust in the high redshift Universe via GRB-DLAs.

Methods. We use absorption-line measured metal column densities for a total of 19 GRB-DLAs, including five new GRB afterglow spectra from VLT/X-shooter. We use the latest linear models to calculate the dust depletion strength factor in each DLA. Using this we calculate total dust and metal column densities to determine a DTM. We explore the evolution of DTM with metallicity, and compare this to previous trends in DTM measured with different methods.

Results. We find significant dust depletion in 16 of our 19 GRB-DLAs, yet 18 of the 19 have a DTM significantly lower than the Milky Way. We find that DTM is positively correlated with metallicity, which supports a dominant ISM-grain-growth mode of dust formation. We find a substantial discrepancy between the dust content measured from depletion and that derived from the total V-band extinction, A_V , measured by fitting the afterglow SED. We advise against using a measurement from one method to estimate that from the other, until the discrepancy can be resolved.

Key words. galaxies:evolution – ISM: dust – ISM: abundances – gamma-ray burst: general

1. Introduction

The abundances and compositions of the dust and metals in the interstellar medium (ISM) can reveal important information about the local environmental conditions. Despite the wealth of information on our doorstep in the ISM of the Milky Way (MW) and Local Group galaxies, it is also necessary to investigate the ISM in the distant Universe, in order to trace its properties in very different environments as well as its evolution over cosmic history.

One of the key constituents of the ISM is dust. It is estimated that up to 30% of all light in the Universe has been reprocessed by dust grains (Bernstein et al. 2002). Dust is necessary for, and traces, star formation across the Universe (Sanders & Mirabel 1996; Genzel et al. 1998; Peeters et al. 2004; Mckee & Ostriker 2007). It also acts as a strong absorber, and its effect must be corrected for when studying sources that shine through it. For example, everything outside the Galaxy must be observed through the dust of the MW, which has a complex topography (Schlafly & Finkbeiner 2011). It is therefore of importance to understand the formation, composition, evolution and observational characteristics of interstellar dust, both in the local and distant Universe. Since dust is intimately connected to the conditions of the ISM and the properties of gas (Draine 2003), the dust-to-gas ratio (DTG, Bohlin et al. 1978) is a good indicator of the dust content of a galaxy or gas cloud. The dust-to-metals

ratio (DTM), which is the DTG corrected for the metallicity of the gas, thus describing the fraction of the total metals that are in the solid dust phase, can reveal more about the nature of the dust itself, its production mechanisms and the processes by which it evolves.

The evolution of the DTM over cosmic time is a tracer of the history of the interplay between gas and dust in the ISM of galaxies, and its distribution in comparison to metallicity can be used to infer clues on the origin of interstellar dust. If all dust and metals were to be produced in and ejected from stars, one would expect the DTM to remain constant in both time and metallicity (e.g. Franco & Cox 1986). In models, this is often assumed (e.g. Edmunds & Eales 1998), and a fairly constant dust-to-metals ratio is indeed observed in the local Universe (Issa et al. 1990; Watson 2011). At higher redshift, Zafar & Watson (2013) found that the DTM in a sample of foreground absorbers to gamma-ray bursts (GRBs) and quasars tends not to vary significantly over a wide range of redshifts, metallicities and hydrogen column densities, proposing a universally constant DTM. Chen et al. (2013) find a slow redshift evolution of DTM in lensed galaxies. These findings suggests that most of the dust is produced ‘instantaneously’ in the ejecta of core-collapse supernova (CC-SNe). These authors all use the traditional method of measuring DTM: the extinction, A_V , is compared to the equivalent metal column density, $\log N(\text{H}) + [\text{M}/\text{H}]$, where $[\text{M}/\text{H}]$ is the logged metallicity of the gas.

Other studies use a different definition of DTM, namely by determining the dust fraction \mathcal{F}_d from the dust depletion (Sect. 2) of metals observed in damped Lyman- α absorbers (DLAs)

[★] Based on observations collected at the European Southern Observatory, Paranal, Chile, Program IDs: 088.A-0051(B), 089.A-0067(B), 091.C-0934, 094.A-0134(A)

on sight lines to quasars (Vladilo 2004; De Cia et al. 2016) and GRBs (De Cia et al. 2013). These studies, contrary to those using A_V as their dust quantifier, claim detections of increasing evolution of the DTM with metallicity. This would suggest that the majority of the dust is formed by growth onto grains in the ISM (Draine 2009), rather than simultaneously together with the metals formed in CCSNe and AGB star envelopes. Tchernyshyov et al. (2015) use depletion observations in the Small Magellanic Cloud (SMC) to suggest the trend between DTM and metallicity only occurs below a certain metallicity threshold that depends on gas density. Mattsson et al. (2014) provide a comprehensive discussion on the debate from a theoretical standpoint, suggesting that selection effects or statistical fluctuations could both explain the differing observed trends, and Feldmann (2015) attempt to model the observed evolution of dust and metal parameters via production, accretion, destruction, as well as gas in-fall and outflow from the galaxy, and also reproduce an evolution of the DTM at low metallicities.

GRBs are a useful tool with which to study trends in the DTM in the distant Universe. They are extremely bright, allowing their detection even at very high redshift (Tanvir et al. 2009), and occur in galaxies with a large range of dust contents and metallicities (e.g. Fynbo et al. 2008; Mannucci et al. 2011; Krühler et al. 2015). GRBs are massive stellar explosions (e.g. Galama et al. 1998), the afterglows of which are observed to have featureless synchrotron spectra (Meszaros & Rees 1997). This means that any absorption lines or changes to the shape of the spectrum must originate from an absorbing medium between the explosion site and the observer. Typically these manifest themselves in the form of DLAs in the host galaxy of the GRB. A DLA is defined as an absorbing system with $\log(N(\text{H I})) > 20.3$ (Wolfe et al. 2005), and it is found that a large proportion of GRB afterglow spectra that lie in the redshift range for the Ly- α transition to fall into the atmospheric transmission window ($z > \sim 1.7$) do indeed fulfill this criterion (e.g. Krühler et al. 2013; Sparre et al. 2014; Friis et al. 2015). With such a large pool of neutral gas, the ionization fraction is small. As such, we can trust measurements of singly ionized metal species to be representative of the total gas phase abundance of these metals in the DLA, and there are numerous collections of such measurements. These measured metal abundances can then be used in a dust depletion analysis in order to measure the DTM.

In this paper, we present spectral analysis of five previously unpublished GRBs, and we combine these with 14 more GRB-DLAs from the literature, all but three of which have mid-to-high resolution spectroscopy. We compute dust depletion curves using all of the available metals, which we then use to calculate average DTM values, and investigate their relation with metallicity and redshift in order to investigate the evolution of DTM.

The structure of this paper is as follows: in Sect. 2 we describe the background and updated methods available to parameterize dust-depletion. The initial sample is presented in Sect. 3. In Sect. 4 we introduce our method of fitting for depletions in GRB-DLAs, and in Sect. 5 we present the results; we discuss the results in Sect. 6 and conclude in Sect. 7. Throughout the paper we assume solar abundances from Asplund et al. (2009).

2. Dust Depletion

Using spectroscopy, it is possible to measure the column density of ISM constituents through absorption lines. However, what one achieves here is a measure of the *gas phase abundance* of that element, as any metal atoms in the dust grains do not contribute to the observed absorption. The difference between the observed

column and intrinsic, total column density of metal X is referred to as *dust depletion*:

$$\delta_X = [X/H]_{\text{obs}} - [X/H]_{\text{in}}, \quad (1)$$

such that the more negative δ_X is, the more of element X is expected to be depleted onto dust grains. We use the standard relative abundance notation,

$$[X/Y] = \frac{\log N(X)}{\log N(Y)} - \frac{\log N(X)_{\text{ref}}}{\log N(Y)_{\text{ref}}}. \quad (2)$$

To calculate the amount of depletion, we need to know two things: the observed gas-phase abundance of each element, and the total intrinsic (gas + dust) abundance. The observed column densities are obtained from the GRB afterglow spectrum, but the intrinsic values are harder to come by, as we do not know *a priori* the total column density of a metal in both the gas and solid phase (i.e. dust). It was shown by Savage & Sembach (1996) that different elements deplete onto dust at different rates. Some, such as Fe and Ni, deplete rapidly, and are known as *refractory* elements. Others, such as Zn and P, are almost always entirely in the gas phase, and are denoted *volatile*. The measured abundance of the volatile element is then a good indicator of the *metallicity* of the system, and the difference in the relative abundances of a volatile and a refractory element, such as the ratio $[\text{Zn/Fe}]$, is thus a basic quantifier of depletion.

Savage & Sembach (1996) measured the depletions of several elements towards a set of different sight lines in the MW, from the dust-poor Warm Halo (WH) clouds, increasing in dust content to Warm Disk+ Halo (WDH), Warm Disk (WD) and finally heavily dusty Cold Disk (CD) clouds. They reported typical depletion levels of each element for each cloud (Fig. 5 and Table 6 in Savage & Sembach 1996). When investigating depletion in a DLA, one can attempt to fit each of the MW depletion patterns to the observed relative abundances. Since the metallicity and dust-to-metals ratio in the DLA are likely to be different to the MW, these are left as free parameters, adjusting the relative abundances expected from the model until they best match those of the observed abundances, a method described by Savaglio (2001) and Savaglio et al. (2003). Despite providing a basis for depletion studies, it is often found that GRB-DLAs tend not to follow any Local Group depletion patterns particularly well (e.g. D’Elia et al. 2014; Friis et al. 2015).

Based on the concept of Savage & Sembach (1996), a more continuous determination of depletion was introduced by Jenkins (2009), based on depletions observed in 17 elements towards stars along 243 MW sight lines. It was found that all elements deplete in a linear fashion, such that the rate of depletion of an element X , δ_X , can be given as:

$$\delta_X = B_X + A_X (F_* - z_X), \quad (3)$$

where A_X is the *depletion slope*, with B_X , z_X as constant offsets. This formulation implies that the difference between the depletion of any two elements should depend only on the value F_* , the *depletion strength factor* of the environment. That is, the relative abundances between any set of two or more elements in a single sight line can only be described by one unique value of F_* , which is then a powerful tool to be able to calculate an overall, average DTM using multiple elements.

In the Jenkins (2009) formulation, $F_* = 0$ is given to those sight lines where the least depletion was observed, with $F_* = 1$ the value for the most depleted MW systems. The F_* method is also applied to the abundances in the Savage & Sembach (1996)

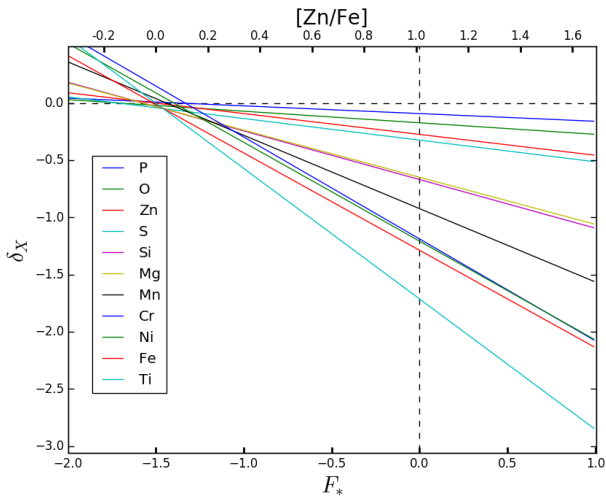


Fig. 1. Depletion δ_X is plotted as a function of F_* . The slope is defined by the parameter B , and the point of zero-depletion by A .

models, with the WH clouds having $F_* = -0.28$, whereas $F_* = 0.90$ in the dusty CD environment.

A study of the Magellanic Clouds (MCs) was presented by Tchernyshyov et al. (2015), using the F_* method to ascertain whether depletion slopes and offsets followed the MW trends from Jenkins (2009). Here, they combined the offsets A_X and z_X into one offset, δ_0 , which simply describes the level of depletion at $F_* = 0$. Compared to the MW, they found differences in the offsets for the elements P, Zn, Si, Cr, and Fe, and that δ_0 decreases with metallicity of the sight line. Depletion slope A_X , however, tends to stay constant. The main interpretation of this is that at lower metallicities, a higher F_* is needed before metals begin to form dust, although this is based on a fairly small sample, covering only the metallicities of the Small and Large Magellanic Clouds.

Recently, the most comprehensive study yet of depletion patterns down to low metallicity and dust content has been conducted by De Cia et al. (2016), detailing depletion sequences of 9 elements in 74 QSO-DLAs at redshifts 1.7-4, and metallicities from the solar value down to $1/100Z_\odot$. Instead of the canonical parameter F_* , they quantify the dust level in any particular DLA with the relative abundances of Zn and Fe, $[Zn/Fe]$. The Zn abundance is corrected for its own depletion by comparing the $[Zn/H]$ and $[Zn/Fe]$ values in the MW. They also include the Jenkins (2009) MW data, in order to provide continuous depletion sequences from the Galactic sight lines right through to the lowest metallicities. As a result, they report updated depletion parameters for these 9 elements: the depletion at $[Zn/Fe] = 0$, A , and the depletion slope, B . These depletion sequences are shown in Fig. 1. There are distinct clusters of elements: P, O, Zn and S, which are volatile elements; refractory elements Cr, Ni and Fe; Si, Mg and Mn, which lie in between the volatile and refractory elements; and Ti, which seems to lie distinctly below all of the others.

From Fig. 1, it can be seen that at $F_* = 0$ there is still significant (~ 1 dex) depletion, especially in the refractory elements, showing that even the least depleted MW clouds are more dusty than those in low metallicity QSO-DLAs. The parameter A can best be seen as the offset in the relative abundance of the element at the point of no iron depletion, $[Zn/Fe]=0$. Since these are all very small, the point at which the depletion starts (i.e. $\delta_X = 0$) is very similar for each element, suggesting that all elements

begin forming dust at some distinct threshold in temperature or density.

The analysis from De Cia et al. (2016) shows that the slopes are linear and well-determined in the whole range from low metallicity, low dust content, right through to the dustiest MW clouds, which we believe is strong evidence that the depletion mechanism works in the same way in all environments, and can indeed always be quantified by a single depletion strength factor. For this reason, we use the slopes from De Cia et al. (2016) for our depletion analysis of the typically low-dust, low-metal GRB-DLA environments.

3. Sample & Data Reduction

In order to select our sample, we require GRBs with mid- to high-resolution spectroscopy, as this allows us to resolve relatively well the velocity structure of the absorber, thus limiting the effect of unidentified saturation in the lines. The spectrum must also cover the Ly- α line, such that we can verify that it is a DLA, and thus regard any ionization correction as negligible. Finally we require that the spectrum includes unsaturated detections of at least four singly ionized metals, in order to increase precision on a measurement of F_* .¹

A state-of-the-art example of an instrument that produces such spectra is X-shooter (Vernet et al., 2011), mounted at ESO's VLT at Cerro Paranal, Chile. X-shooter operates simultaneously in 3 spectral arms, namely the bands UVB (3000-5500 Å), VIS (5500-10000 Å), and NIR (10000-25000 Å), thus allowing absorption line metallicity measurements from redshifts ≥ 1.8 , and providing a wide spectral range. It operates at a resolving power of around $R = 8000$, depending on the arm, slit used and atmospheric conditions. 12 GRBs observed with X-shooter pass our selection criteria. Seven of these, GRBs 090809, 090926A, 100219A, 111008A, 120327A, 120815A and 121024A (references in Table 1), have already been published in the literature, and we include them in the sample. In this paper we present the analysis for the remaining five: 120119A, 120716A, 120909A, 130408A² and 141028A, the details of which are given in Sect. 3.1. A further two GRBs observed with UVES pass the selection criteria (050730 and 081008, both taken from the literature), and an additional two GRBs observed with Keck HIRES and ESI have data published and are therefore also included in sample (050820A and 000926 respectively). Unpublished GRBs with Keck high resolution spectral data cannot be included in the sample since data are not public. In order to help populate the sample with dust-rich sight lines, we add three low-resolution (VLT/FORS) spectra of GRBs 050401, 070802 and 090323, which have high $N(H)$, high A_V and high metallicity respectively. However, given the uncertainty in the derived column densities for these GRBs, we distinguish them from the rest of the sample when presenting our results. The final sample of 19 GRBs is presented in Table 1, with HI measurements given in Table 2.

¹ We select GRBs up until the end of 2014. There are more recent GRBs that also pass the selection criteria, but it is beyond the scope of this paper to keep adding to the sample.

² Spectra of GRBs 120716A, 120909A and 130408A were analyzed by Cucchiara et al. (2015), but that work presented column density measurements for only Ly- α and one other element.

Table 1. Hydrogen and metal abundances in our sample of GRB afterglows. Units of column density are $\log(\text{cm}^{-2})$.

GRB	z	$\log N(\text{Mg})$	$\log N(\text{Si})$	$\log N(\text{P})$	$\log N(\text{Ti})$	$\log N(\text{Cr})$	$\log N(\text{Mn})$	$\log N(\text{Fe})$	$\log N(\text{Ni})$	$\log N(\text{Zn})$	$\log N(\text{S})$
000926	2.04	-	16.47 ± 0.05^1	-	-	14.34 ± 0.05^1	-	15.60 ± 0.20^1	-	13.82 ± 0.05^1	-
050401	2.9	-	16.5 ± 0.4^2	-	-	14.6 ± 0.2^2	-	16.0 ± 0.2^2	-	14.3 ± 0.3^2	-
050730	3.9672	$< 16.08^4$	15.47 ± 0.03^4	-	-	-	-	15.49 ± 0.03^3	13.69 ± 0.02^3	-	15.11 ± 0.04^3
050820A	2.6145	15.86 ± 0.05^4	-	13.64 ± 0.04^4	-	13.33 ± 0.02^4	-	14.82 ± 0.12^4	13.69 ± 0.04^4	12.96 ± 0.02^4	15.57 ± 0.04^4
070802	2.45	-	16.00 ± 0.32^5	-	-	14.04 ± 0.40^5	13.69 ± 0.18^5	16.16 ± 0.18^5	14.89 ± 0.28^5	13.67 ± 0.65^5	-
081008	1.9685	-	15.75 ± 0.04^6	-	-	13.83 ± 0.03^6	-	15.42 ± 0.04^6	13.74 ± 0.07^6	13.15 ± 0.04^6	-
090323	3.567	-	15.80 ± 0.05^7	-	-	-	-	15.00 ± 0.05^7	14.76 ± 0.04^7	13.57 ± 0.04^7	-
090809	2.737	$> 16.80^8$	16.15 ± 0.07^8	-	-	-	13.75 ± 0.12^8	15.75 ± 0.07^8	14.40 ± 0.07^8	13.70 ± 0.25^8	15.80 ± 0.02^7
090926A	2.1071	$> 14.11^9$	14.80 ± 0.08^9	-	-	-	-	15.00 ± 0.05^7	14.40 ± 0.07^8	-	-
100219A	4.667	$> 13.72^{10}$	15.25 ± 0.25^{10}	-	-	-	-	14.86 ± 0.09^9	13.92 ± 0.13^9	-	14.89 ± 0.10^9
111008A	4.99	-	$> 15.86^{11}$	-	-	-	-	14.73 ± 0.11^{10}	-	-	15.25 ± 0.15^{10}
120119A	1.7285	-	16.67 ± 0.03^{12}	-	-	14.17 ± 0.11^{11}	13.72 ± 0.08^{11}	16.05 ± 0.05^{11}	14.89 ± 0.18^{11}	13.28 ± 0.21^{11}	15.71 ± 0.09^{11}
120327A	2.8145	16.34 ± 0.02^{13}	16.36 ± 0.03^{13}	-	13.18 ± 0.04^{12}	14.21 ± 0.07^{12}	13.99 ± 0.01^{12}	15.95 ± 0.03^{12}	14.77 ± 0.02^{12}	14.04 ± 0.04^{12}	-
120716A	2.487	-	16.48 ± 0.21^{12}	14.19 ± 0.04^{13}	-	14.17 ± 0.02^{13}	-	15.78 ± 0.09^{13}	14.61 ± 0.09^{13}	13.40 ± 0.04^{13}	15.74 ± 0.02^{13}
120815A	2.358	-	$\geq 16.34^{14}$	-	-	14.20 ± 0.06^{12}	14.02 ± 0.08^{12}	15.65 ± 0.05^{12}	14.42 ± 0.06^{12}	13.91 ± 0.10^{12}	-
120909A	3.929	$\leq 16.55^{12}$	$\leq 16.22 \pm 0.03^{12}$	-	-	13.75 ± 0.06^{14}	13.26 ± 0.05^{14}	15.29 ± 0.05^{14}	14.19 ± 0.05^{14}	13.47 ± 0.06^{14}	$\leq 16.22^{14}$
121024A	2.30	-	$> 16.35^{15}$	-	-	-	-	15.20 ± 0.06^{12}	14.30 ± 0.02^{12}	13.55 ± 0.08^{12}	15.91 ± 0.06^{12}
130408A	3.7579	16.01 ± 0.21^{12}	15.95 ± 0.09^{12}	-	12.77 ± 0.08^{12}	14.18 ± 0.03^{15}	13.74 ± 0.03^{15}	15.82 ± 0.05^{15}	14.70 ± 0.06^{15}	13.74 ± 0.03^{15}	$> 15.90^{15}$
141028A	2.333	15.28 ± 0.27^{12}	14.82 ± 0.08^{12}	-	-	13.81 ± 0.06^{12}	13.19 ± 0.07^{12}	15.52 ± 0.09^{12}	14.15 ± 0.04^{12}	12.87 ± 0.09^{12}	15.78 ± 0.18^{12}
				-	-	12.98 ± 0.30^{12}	$< 13.29^{12}$	14.23 ± 0.04^{12}	13.34 ± 0.20^{12}	12.38 ± 0.22^{12}	-

References. (1) Savaglio et al. (2003); (2) Watson et al. (2006); (3) Ledoux et al. (2009); (4) Prochaska et al. (2007); (5) Elíasdóttir et al. (2009); (6) D'Elia et al. (2011); (7) Savaglio et al. (2012); (8) Skúladóttir (2010); (9) D'Elia (2010); (10) Thöne et al. (2013); (11) Sparre et al. (2014); (12) *this work*; (13) D'Elia et al. (2014); (14) Krühler et al. (2013); (15) Frits et al. (2015)

3.1. New GRB Spectra

For the spectra of GRBs 120119A, 120716A, 120909A, 130408A and 141028A we perform our own analysis on the spectra obtained from X-shooter. The general method to reduce the raw spectra is based on the standard X-shooter pipeline (Goldoni et al. 2006; Modigliani et al. 2010), which we modify in accordance with procedures outlined in Krühler et al. (2015), including a correction for telluric absorption using the Molecfit software (Smette et al. 2015). To normalize, we select points on the continuum unaffected by absorption lines, and fit a spline function. Due to good seeing, the resolution of the spectrum is often larger than the instrumental resolution as determined from arc lamp exposures (see e.g. Krühler et al. 2013). We therefore follow the standard procedure which is to measure the velocity resolution from unsaturated, single telluric lines. Since there are no telluric lines in the UVB, we use the resolution of those measured in the other two arms, calculating the resolution in the UVB using known conversion factors in line with Fynbo et al. (2011). We perform Voigt-profile fits on the absorption lines using the line-fitting software VPFit³. We determine the nature of any velocity components using singly ionized, unsaturated and unblended lines, with e.g. Fe II λ 1611, Ni II λ 1751, 1741, Si II λ 1808 and Mn II λ 2606 often useful transitions. We then fix redshift, z , and broadening parameter, b km s⁻¹, for each velocity component across all species, leaving column density N cm⁻² as the free parameter. We present the resulting column densities in Table 1, and present a selection of line fits for each GRB in Appendix A.

4. Method

4.1. Depletion Model Fitting

Using the concept of linear depletion sequences and F_* from Jenkins (2009), De Cia et al. (2016) use the observable $[Zn/Fe]$ as their dust indicator. One can directly translate between the two with the relation $F_* = 1.48 \times [Zn/Fe] - 1.50$. To avoid confusion between $[Fe/Zn]$ as an intrinsic measured value, and "adjusted" $[Fe/Zn]$ as a dust indicator, we use the De Cia et al. (2016) depletion models, but with F_* as our depletion strength factor. For a given metallicity and dust depletion strength, the relative abundance in element X that according to the model we expect to measure is thus:

$$[X/H]_{\text{exp}} = \delta_X + [M/H] = A + B \frac{(F_* - 1.50)}{1.48} + [M/H], \quad (4)$$

where $[M/H]$ is the metallicity of the system. We vary F_* and $[M/H]$ to minimise the χ^2 parameter between the observed abundances and those expected from the model, thus achieving a best fit depletion strength and metallicity. The 1σ errors on the parameters are calculated for a single parameter of freedom.

The errors on F_* and $[M/H]$ are dependent on both the errors on the column densities of each individual element, and on the number of elements included in the dust depletion curve fits. Therefore, when only 4 elements are available, or when the column density measurements are not tightly constrained, the uncertainty on the metallicity and F_* can be quite large. The 2D chi-squared contour plots are provided in Appendix B. The shape of these show elongate confidence regions, which can be seen as a degeneracy between the two parameters. In most cases F_* and $[M/H]$ are still well constrained, and when this is not the case it is reflected in large errors, for example in GRB 050401.

³ VPFit: <http://www.ast.cam.ac.uk/rfc/vpfit.htm>

Unfortunately, De Cia et al. (2016) did not include measurements for Ni or Ti. Ni in particular is measured in the majority of our spectra, and as a strongly refractory element with depletion properties similar to Fe, provides valuable information on the dust content of the DLA. We therefore follow the procedure they use to calculate their Zn depletion as a function of $[Zn/Fe]$ in the Galaxy only, using Ni and Ti column densities from Jenkins (2009) and orthogonal distance regression to linearly fit the data. We have seen that the slopes measured down to low dust content are compatible with those measured only in the Galaxy to within uncertainties, and as such trust that our Ni and Ti A and B values also follow this trend, and provide model values consistent with those for the other elements.

4.1.1. Nucleosynthesis

Dust depletion analysis relies on the difference between an observed and an expected, intrinsic abundance, for each metal. As standard, we use solar abundances from Asplund et al. (2009) as our reference. This could, however, lead to errors in the depletion calculation. Similar to the composition of dust grains, it is perfectly logical to assume that intrinsic abundances in a high redshift DLA are somewhat different to those observed in the Sun.

One of the most common nucleosynthetic effects at high-redshift and low metallicity is an overabundance of α -elements such as O, Si, S and Mg, in comparison to Fe, often denoted by the factor $[\alpha/Fe]$. The De Cia et al. (2016) depletion patterns have been corrected for these effects, and we adopt their method of applying corrections in our work. In short, this involves applying the observed trend between $[Zn/Fe]$ and $[Zn/H]$ to use $[Zn/Fe]$ as a basic proxy for metallicity. We then correct our observed relative abundance $[X/H]$ depending on the estimated metallicity of the system, using the slopes provided in De Cia et al. (2016), Fig. 7.

Vladilo et al. (2011) go about calculating the reference abundances in a more theoretical way, using galaxy evolution models to predict metal abundances. It would be interesting to see how such an approach affected our results, but such an analysis is beyond the scope of this paper.

4.2. Dust-to-Metals Ratio

Rather than comparing dust and metal quantities measured by different means (e.g. Zafar & Watson 2013), or by using only one refractory element to trace the dust, we use the depletion strength factor F_* along with our best fit $[M/H]$ and measured $N(H)$ to calculate the total column densities in dust phase for all 11 elements, including those not measured in the spectrum:

$$N(X)_{\text{dust}} \approx N(H) 10^{[X/H]_{\odot}} 10^{[M/H]} (1 - 10^{\delta_X}) \text{cm}^{-2}. \quad (5)$$

We can then sum over the elements to find the total dust column density in terms of atoms in the dust phase per cm².

$$N(\text{dust}) \approx N(H) \sum_X \frac{Z}{Z_{\odot}} 10^{[X/H]_{\odot}} (1 - 10^{\delta_X}) \text{cm}^{-2}, \quad (6)$$

and similarly for the total metal column:

$$N(\text{metals}) \approx N(H) \sum_X \frac{Z}{Z_{\odot}} 10^{[X/H]_{\odot}} \text{cm}^{-2}, \quad (7)$$

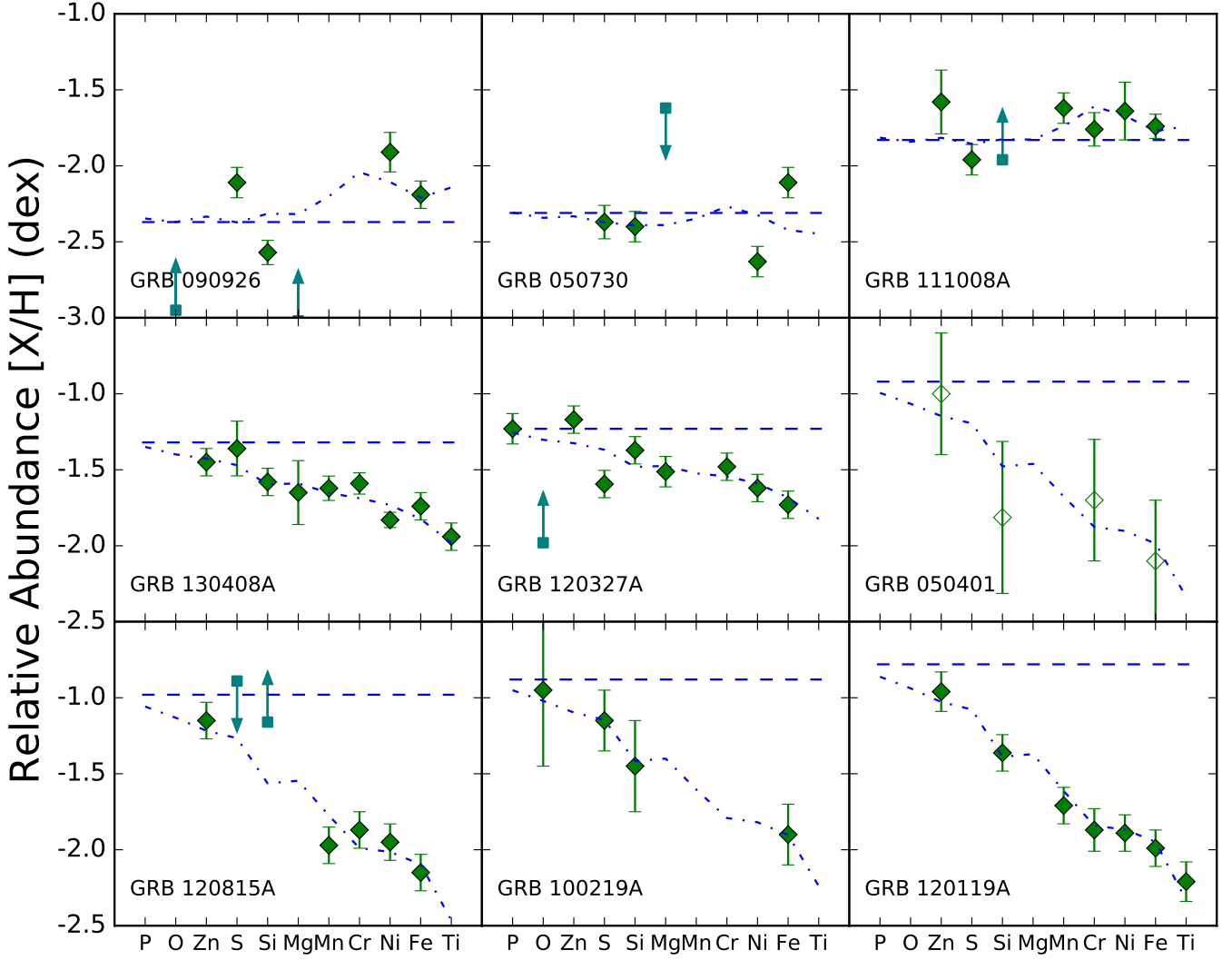


Fig. 2. Dust depletion fits for the nine lowest metallicity GRB-DLAs in our sample. The diamond points are the observed relative abundances, the dot-dashed line follows the expected depletion at a strength of the best fit F_* , and the dashed line represents the best fit metallicity. Unfilled markers represent low-resolution spectral data, and squares with up (down) arrows represent lower (upper) limits.

with $Z/Z_\odot = 10^{[M/H]}$. We then take the ratio between the dust and total metal column densities, to find a dust-to-metals ratio for the DLA. We can see that metallicity and $N(\text{H})$ cancel out, such that the DTM calculation is independent of the best fit metallicity and hydrogen column density.

$$\text{DTM} = \frac{N(\text{dust})}{N(\text{metals})} = \frac{\sum_X 10^{[X/H]_\odot} (1 - 10^{\delta_X})}{\sum_X 10^{[X/H]_\odot}}, \quad (8)$$

As is customary in DTM analysis, we normalize our values to that of the MW. We compute a Galactic DTM using the same procedure as outlined above, assuming an F_* of 0.5, as this is the average found in the 243 J09 lines of sight. We denote the MW-normalized value as \mathcal{DTM} .

We calculate the error on \mathcal{DTM} by propagating those from the best fit depletion through Eq. 8. In particular, the error on the metal fraction, 10^{δ_X} , is $10^{\delta_X} \ln 10 \alpha_{\delta_X}$, where α_{δ_X} is the error on the depletion in X . This is then propagated in quadrature with those from the reference abundances.

5. Results

The depletion curves for each GRB-DLA are shown in Figs. 2 and 3, the results of which are presented in Table 2, including output values for F_* , metallicity, and dust-to-metals ratio.

5.1. Metallicity

We present dust-corrected metallicities for the 19 GRB-DLAs, including 5 previously unpublished objects. The metallicities range from the very metal-poor $[M/H] = -2.37$ in GRB 090926A to the super-solar $[M/H] = 0.41$ in GRB 090323, with a median of $[M/H] = -0.63$, which is equal to $0.25 Z_\odot$, similar to the SMC. The metallicities for all of the GRBs in this sample were presented by Cucchiara et al. (2015) using the apparent optical depth (AOD) method to measure column density. Our metallicities tend to agree with those from that work, although they are typically slightly higher, due to the fact that we make a correction for dust depletion. They find a weak decrease in metallicity with redshift. The metallicity as a function of redshift for our sample is shown in Fig. 4. There is no significant trend, although we do note that excluding the low-resolution, super-solar data

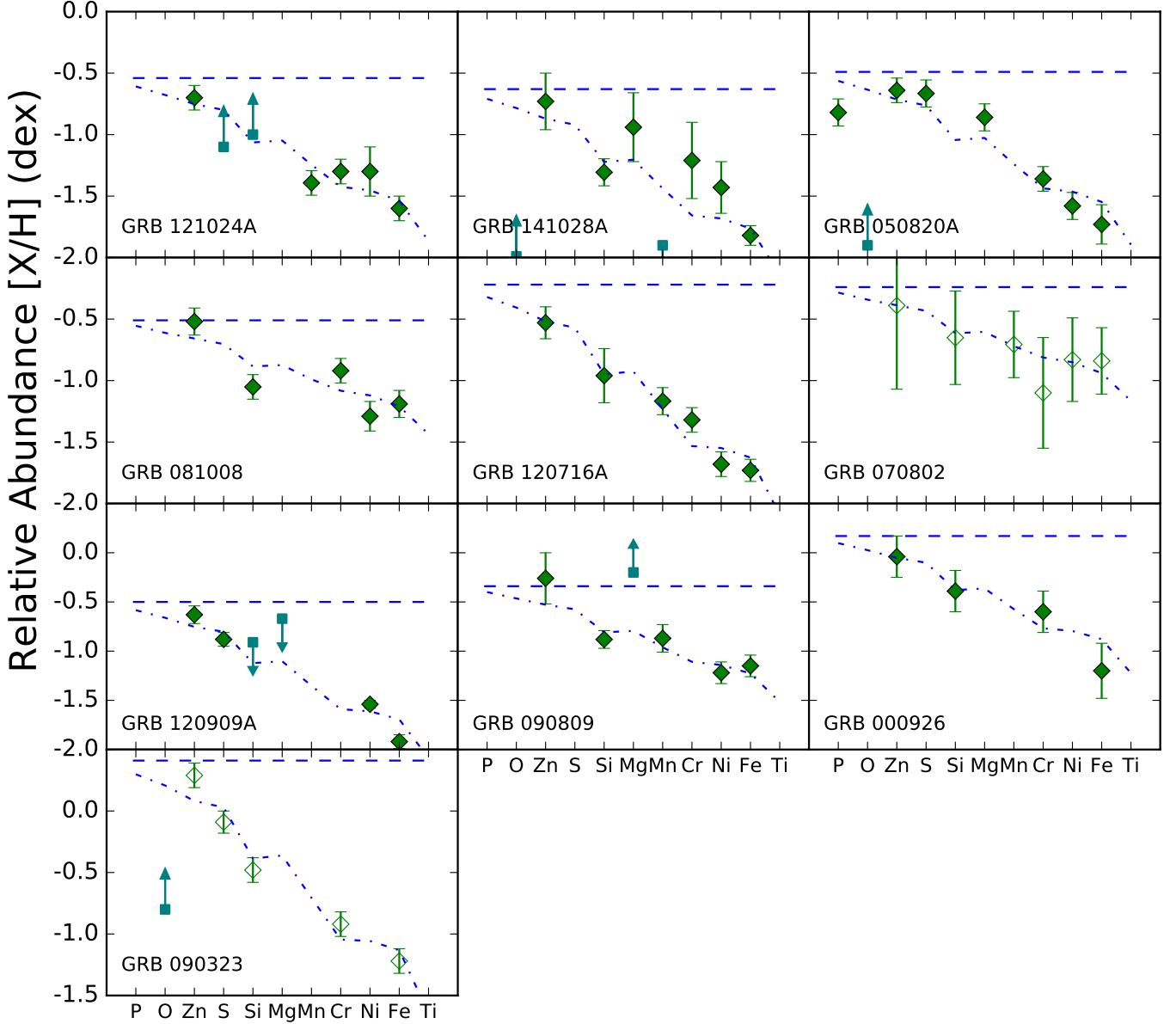


Fig. 3. A continuation of Fig. 2 for the ten GRB-DLAs with highest metallicity.

point at redshift 3.6, there could be a slight decrease in metallicity with redshift, as one would expect given the evolution of galaxies over cosmic time.

The metallicities we derive tend to have a larger uncertainty than those often quoted for GRB-DLAs. Most published metallicities do not account for dust depletion, assuming that volatile elements are good metallicity tracers as they do not deplete strongly into dust. We quote our metallicities with the knowledge that even the most volatile elements deplete to some degree, and in a linear fashion with F_* , thus giving rise to a larger uncertainty due to a degeneracy between $[M/H]$ and F_* . We note that GRBs with detections of numerous species tend to produce a smaller uncertainty on the metallicity than those with only four, since the degeneracy can better be disentangled.

5.2. Dust-to-Metals ratio

The F_* values have a mean of -0.53, which equates to a $[Zn/Fe]$ of 0.66, 0.6 dex lower than the mean Galactic value of 1.22. This is reflected in a mean DTM of 0.62, while the median is 0.74. The standard deviation of DTM is 0.27, such that the mean differs from the Galactic DTM by nearly 2σ while the median is lower at just below 1σ significance. This result is similar to the QSO-DLA results from De Cia et al. (2016), whose mean and standard deviation are 0.70 and 0.26 respectively. GRB 090926A is the only DLA which shows no dust depletion with $F_* = -1.7$, which lies to the left of the point where all the depletion slopes cross the axis of zero depletion in Fig. 1.

Fig. 5 shows the DTM plotted against redshift. From this small sample, we don't see any significant trend with redshift. This result is consistent with the hydrodynamical simulations of McKinnon et al. (2016), who find no evolution in the DTM at redshifts $z \geq 1$. In Fig. 6, we plot our DTM against

Table 2. Results of the fitting of the F_* depletion model to metal column densities from 19 GRB-DLAs. Given uncertainties are at the 1σ level.

GRB	A_V (mag)	$\log(N(\text{H}) \text{ cm}^{-2})$	F_*	[M/H]	\mathcal{DTM}
000926	0.38 ± 0.05^1	21.30 ± 0.20	-0.28 ± 0.18	0.17 ± 0.34	0.76 ± 0.07
050401	0.45 ± 0.035^2	22.60 ± 0.30	-0.26 ± 0.31	-0.92 ± 0.68	0.76 ± 0.09
050730	$\leq 0.17^2$	22.10 ± 0.10	-1.38 ± 0.07	-2.31 ± 0.18	0.19 ± 0.02
050820A	0.27 ± 0.05^3	21.05 ± 0.10	-0.27 ± 0.07	-0.49 ± 0.10	0.76 ± 0.06
070802	1.23 ± 0.05^4	21.50 ± 0.20	-0.69 ± 0.18	-0.24 ± 0.80	0.59 ± 0.06
081008	$\leq 0.08^4$	21.11 ± 0.10	-0.69 ± 0.06	-0.51 ± 0.17	0.59 ± 0.04
090323	0.10 ± 0.04^2	20.72 ± 0.09	0.30 ± 0.07	0.41 ± 0.11	0.95 ± 0.07
090809	0.11 ± 0.04^5	21.40 ± 0.08	-0.47 ± 0.07	-0.34 ± 0.25	0.68 ± 0.05
090926A	$\leq 0.01^6$	21.60 ± 0.07	-1.7 ± 0.07	-2.37 ± 0.16	0.00 ± 0.01
100219A	0.15 ± 0.03^7	21.14 ± 0.15	-0.31 ± 0.22	-0.88 ± 0.33	0.74 ± 0.07
111008A	0.10 ± 0.05^7	22.30 ± 0.06	-1.58 ± 0.06	-1.83 ± 0.16	0.05 ± 0.01
120119A	1.06 ± 0.02^8	22.44 ± 0.12	-0.14 ± 0.06	-0.78 ± 0.18	0.80 ± 0.06
120327A	$\leq 0.02^8$	22.01 ± 0.09	-0.92 ± 0.05	-1.23 ± 0.08	0.44 ± 0.03
120716A	0.30 ± 0.15^5	21.88 ± 0.08	0.15 ± 0.05	-0.22 ± 0.22	0.90 ± 0.06
120815A	0.08 ± 0.02^8	21.95 ± 0.10	-0.20 ± 0.07	-0.98 ± 0.22	0.78 ± 0.06
120909A	0.16 ± 0.04^8	21.61 ± 0.06	-0.11 ± 0.04	-0.50 ± 0.10	0.82 ± 0.06
121024A	0.21 ± 0.03^8	21.85 ± 0.15	-0.34 ± 0.06	-0.54 ± 0.18	0.73 ± 0.05
130408A	0.22 ± 0.03^8	21.76 ± 0.03	-0.92 ± 0.03	-1.32 ± 0.11	0.47 ± 0.03
141028A	0.13 ± 0.09^5	20.55 ± 0.07	-0.18 ± 0.07	-0.63 ± 0.26	0.79 ± 0.06

References. (1) Starling et al. (2007); (2) Schady et al. (2011); (3) Schady et al. (2012); (4) Greiner et al. (2011); (5) *this work*; (6) Rau et al. (2010); (7) Bolmer et al. *in prep*; (8) Greiner et al. *in prep*

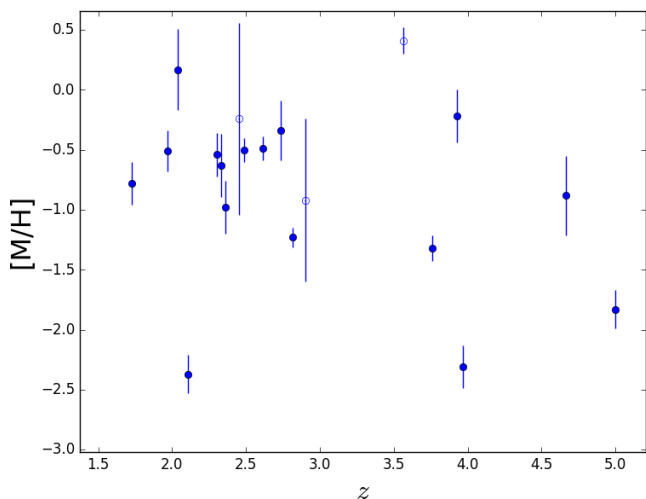


Fig. 4. The metallicity [M/H] as a function of redshift. Open samples are those taken from low-resolution spectra.

metallicity, and find a positive correlation between the two with a Spearman's Rank of $\rho = 0.63$, which with 19 data pairs leads to a false-correlation probability of 0.004. There is a potential flattening of the relation, such that above [M/H] = -1 there is no real correlation. The potential reasons for this are discussed in the following section.

6. Discussion

6.1. The Origin of Dust

Fig. 6 shows that the dust-to-metals ratio increases with metallicity. Typically, this would support the view that the dust is formed by grain growth in the ISM (Draine 2009). Mattsson et al. (2014) can also explain this scenario in terms of dust

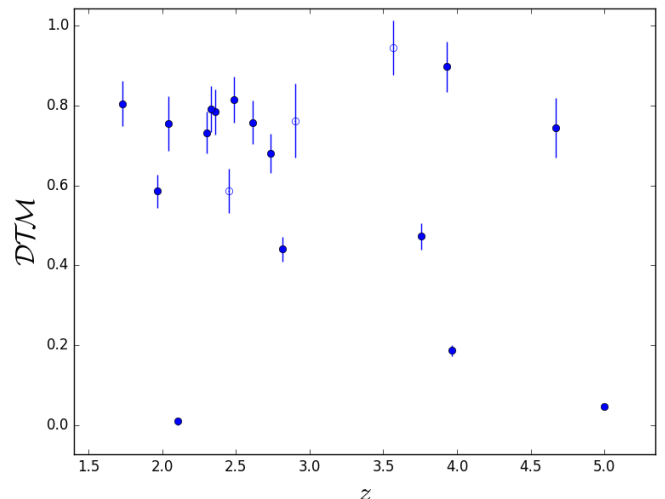


Fig. 5. The \mathcal{DTM} as a function of redshift. z error bars are too small to be displayed. There does not seem to be any evolution over the redshift range of 1.7-5, but no conclusions can be drawn with such a small sample.

created in stars and supernovae, and then kept in balance by ISM grain growth counteracting dust destruction mechanisms. We also notice a potential flattening of this trend above metallicities of $0.1Z_{\odot}$. This flattening seems opposite to what is predicted in the models of Mattsson et al. (2014) and Mattsson (2016), in which the DTM is fairly constant (and low) until a critical metallicity of $0.1Z_{\odot}$ at which point dust production via grain growth is kick-started and the DTM grows towards the Galactic value at solar metallicity. Our observed trend could instead be explained by a higher rate of dust destruction at lower metallicities. As noted in De Cia et al. (2013), this could be due to the star forming environments that GRBs are known to

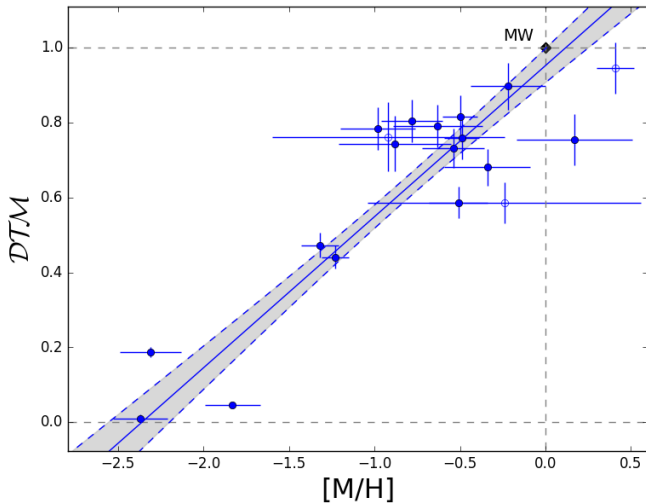


Fig. 6. \mathcal{DTM} as calculated using Eq. 8 as a function of metallicity. The dashed line and shaded area is a linear fit to the data and its 1σ confidence interval respectively, tracing a significant positive correlation between the two variables. The trend is predominantly set by the lowest metallicity points, with those data points at $[M/H] > -1$ showing no obvious trend. The Milky Way is shown by a black point at $[M/H]=0$, $\mathcal{DTM}=1$.

trace (e.g. Savaglio et al. 2009), the strong radiation fields in such environments produced by young OB stars and shocks from supernovae (SNe), which may destroy dust faster than it can be created by grain growth when the metallicity is low. The higher metallicity DLAs in our sample could be located at greater distances from the GRB itself, or even in outflows from the host galaxy, where star-formation could be lower and as such may harbour lower radiation and fewer shocks, allowing the ISM growth to replenish dust to the equilibrium level. It would be interesting to investigate excited lines and velocity profiles in more detail to establish any trends between neutral gas metallicity and DTM, and distance from the GRB explosion site, but such a study would require a larger sample of GRBs with time-varying fine structure line observations.

The amount of dust along the line of sight can also be measured by the effect it has on the spectral energy distribution (SED) of a GRB afterglow. Specifically, the SED is ‘reddened’, and this reddening can be expressed as the total extinction in the V -band, A_V . The values for $A_{V;SED}$ are found by fitting broadband SEDs from the optical to the X-ray regimes (see e.g. Greiner et al. 2011; Schady et al. 2012; and upcoming papers Bolmer et al. and Greiner et al, both *in prep*). For all bursts from 2007 onwards, we use optical/NIR data from the 7-channel imager GROND (Greiner et al. 2008), and X-ray data from the X-ray Telescope (XRT; Burrows et al. 2005) on board *Swift* (Gehrels et al. 2004). For the pre-GROND bursts, see Schady et al. (2011). A simple power-law or broken power-law is fit to the observed data, and ‘missing’ flux in the bluer visible bands attributed to dust. This reddening is fit with one of 3 different extinction laws, namely those from the SMC, LMC and MW (Pei 1992), and is described by the colour excess, $E(B - V)$. This is converted into $A_{V;SED}$ via the relation of:

$$A_V = R_V E(B - V). \quad (9)$$

R_V is the total-to-selective extinction, and is fairly well known for the Local Group extinction curves, at an average of 3.08,

3.16 and 2.93 for the MW, LMC and SMC respectively. It depends largely on the grain-size distribution. Typically, these Local Group extinction laws produce a good fit to GRB SEDs (Schady et al. 2010; Kann et al. 2010; Greiner et al. 2011), and although the best-fit A_V varies slightly depending on which curve is used, such measurements are robust representations of $A_{V;SED}$.

In Fig. 7, we plot the metals-to-dust ratio according to the definition of Zafar & Watson (2013), which uses the A_V as a dust tracer. Similar to that work, we see no strong trend with metallicity, at odds with the result from Fig. 6. We do note that our mean metals-to-dust of $21.65 \text{ cm}^{-2} A_V \text{ mag}^{-1}$ is higher than that from their sample, and we see a higher spread of $\sigma = 0.46$ dex. A Spearman’s Rank test gives $\rho = 0.38$, with a false positive probability of $P = 0.11$, suggesting that there is perhaps a slight positive correlation, and indeed in the opposite direction to that in our \mathcal{DTM} method. Given that the metal measurement is coming from the same place in both methods, there must be a discrepancy between how the dust is measured, the reasons for which we explore in the following sections.

6.2. The $A_{V;SED}$ to $A_{V;DTM}$ Discrepancy

We can see from Figs. 6 and 7 that depletion and extinction seem either to have different sensitivity, or do not trace the same dust along the line of sight, or properties thereof. To compare these we look to the relation used to calculate a value of A_V from a depletion-measured DTM, which we label $A_{V;DTM}$. This is based on the average extinction for a given hydrogen column density in the MW, scaled for DTM and metallicity, as per Savaglio et al. (2003), and using the $N(\text{H})/A_V$ from Watson (2011).

$$A_V = 0.45 \frac{\mathcal{DTM}}{\mathcal{DTM}_{\text{Gal}}} \frac{Z}{Z_{\odot}} \frac{N(\text{H}) \text{ cm}^{-2}}{10^{21}} \text{ mag}, \quad (10)$$

with $N(\text{H})$ measured in cm^{-2} . In the literature there are many cases of GRB afterglows where a direct A_V measurement from the SED was possible, as well as spectra with measurable depletion, and there is often disagreement between the two values, with the depletion-inferred A_V usually higher than the SED value (e.e. Watson et al. 2006; Savaglio et al. 2012; Friis et al. 2015). For our sample, we compare our independently measured $A_{V;SED}$ values to $A_{V;DTM}$ based upon the \mathcal{DTM} , $N(\text{H})$ and $[M/H]$ from our fits, the result of which is shown in Fig 8. There seem to be two distinct groups of objects: (1), the group above the green 1:1 line which make up the majority of the sample, which show the known over prediction of $A_{V;DTM}$ compared to $A_{V;SED}$, and are best fit by the blue dashed line; and (2), those below the line, which are those whose $A_{V;DTM}$ prediction is lower than that measured from the SED. These include the known outlier GRB 070802 (Krühler et al. 2008; Elíasdóttir et al. 2009), at an $A_{V;SED}$ of 1.23 mag. This under prediction for GRB 070802 is also noted by De Cia et al. (2016), and could be a result of the uncertain column density measurements resulting from low-resolution spectral data.

Including those with $A_{V;SED}$ upper limits, 11 GRBs sit as over predictions in group (1), while 6 are definitely in group (2). Of these, one is GRB 070802. The others are GRBs 050820A, 100219A, 111008A, 130408A and 141028A. GRB 090926A shows negligible dust in both depletion and extinction.

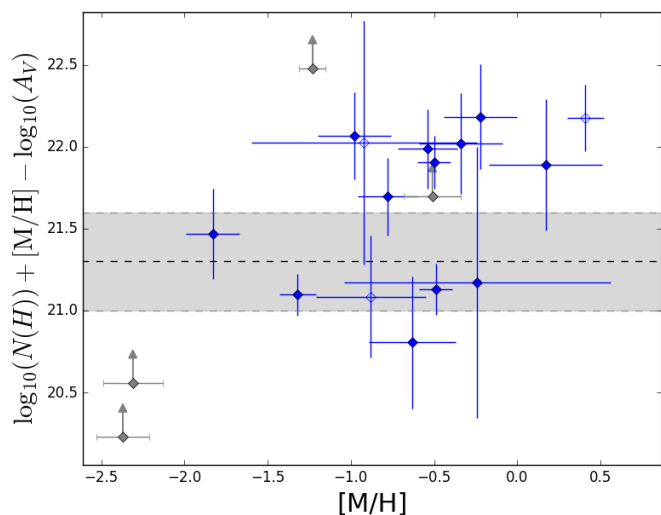


Fig. 7. The metals-to-dust diagnostic used by Zafar & Watson (2013), as applied to our data along with the Local Group average and standard deviation that they quote (Dashed line and shaded area).

6.3. Accuracy of $A_{V;DTM}$ - Depletion As A Reliable Tracer of Dust

A potential reason for the discrepancy is touched upon in Zafar & Watson (2013), who mention that while depletion is often based upon Fe, the vast majority of dust mass is composed of O, C, Mg and Si, arguing that Fe-based depletion measurements may not correctly trace most of the dust. Indeed, Dwek (2016) provide a compelling argument for Fe dust production being different to that of the bulk of the elements; namely being formed by cold grain growth in the ISM compared to CCSNe and post-AGB star envelopes. In this argument, depletion based upon iron measurements is therefore bound to trace different dust to extinction. However, the linear depletion sequences seen by Jenkins (2009) and De Cia et al. (2016) show that by calculating the F_* for a particular line of sight, we can get a robust prediction for dust fractions and columns for all elements, including those not measured in the DLA, and thus we are incorporating not only the dust compounds traced by iron, but also the silicates and carbonaceous grains as well.

We have followed the procedure in De Cia et al. (2016) to correct relative abundances for nucleosynthetic effects, such that any discrepancies between our adopted intrinsic abundance and that true to the DLA are likely to be marginal, and certainly not enough to cause the observed offset in the $A_{V;DTM}$ prediction.

6.4. Accuracy of $A_{V;SED}$

Assuming that our depletion measure is indeed a solid representation of the total dust column, we look to $A_{V;SED}$ for the reason as to why there could be a discrepancy. The question one may ask is whether the Local Group extinction curves are a good fit for GRB-DLAs, or whether one should use something other than the MW, LMC or SMC as their model. Indeed, Friis (2015) claim that grey dust extinction, so called because the extinction is weakly dependent on wavelength, could be prominent in up to as many as 25% of GRB-DLAs, including GRB 121024A which is included in our sample. Their reasoning is that a top-heavy grain-size distribution would cause a very flat extinction curve. When fitting a broken power-law SED, there is then a degeneracy between the steepness of the extinction curve (i.e. the A_V),

and the position of the break between X-ray optical power-law slopes (Schady et al. 2012), with one of the solutions being a large amount of grey dust, which corresponds to a large A_V for a small $E(B-V)$. If the extinction in our group (1) DLAs were to be caused by grey dust, then we may be able to reconcile the over-predicted $A_{V;DTM}$ with $A_{V;SED}$. However, some of these show compelling evidence for the contrary:

GRB 120327A is best fit by a simple power law and an SMC-like extinction of $A_{V;SED} = 0.05$ mag, with $A_{V;DTM} = 0.18$ mag. The power law removes any degeneracy in the slope of the dust extinction law, and thus excludes the possibility of significant grey dust. Another example is GRB 120815A, whose $A_{V;SED} = 0.08$ mag, fit by a power law and SMC-like extinction, is significantly smaller than $A_{V;DTM} = 0.44$ mag. We find that GRB 121024A is also best fit with a power law. Indeed, Fig. 8 shows that only one object that has an over-predicted A_V was fit with a broken power law.

For the group (2) objects, we notice that 050820A, 100219A, 111008A, and 130408A all have intervening absorbing systems. Should these have a high dust content, they could significantly affect the SED of the GRB afterglow, such that the reddening caused by dust in the host galaxy itself is indeed smaller, thus pushing these objects towards the 1:1 line. However, for these intervening systems to be the reason for a much higher $A_{V;SED}$ than from DTM, they would need to contribute around 80% of the extinction along the line of sight, whereas these systems are typically much weaker in metal line absorption than the host DLA (e.g. in GRB 100219A, Thöne et al. 2013). We therefore find it unlikely that a significant amount of the extra extinction is caused by intervening systems.

6.5. The equivalent dust column density

Having established that depletion is a good tracer of the dust, and in particular the best tracer of the dust-to-metals ratio, and $A_{V;SED}$ being accurate and reliable, we look to the relation used to calculate $A_{V;DTM}$, Eq. 10. This is based upon the relation between hydrogen and dust in the Galaxy, where a column of $N(H) = 10^{21} \text{ cm}^{-2}$ results in an A_V of 0.45. We note that the value of the Galactic gas-to-dust ratio varies depending on the sample and technique used to measure it. We use the result of Watson (2011). Measurements of this value have been consistent over the past few decades, and include those by Bohlin et al. (1978), Predehl & Schmitt (1995), and Güver & Özel (2009). The value used does not alter the fact that a significant discrepancy is observed. In DLAs, the hydrogen column density is scaled for dust-to-metals ratio and metallicity, to take into account the differing dust-to-gas ratios in such environments. However, the over- and under predictions in Fig. 8 show that the scaling between this equivalent dust column density and the A_V may well be wrong. That is to say that in DLAs, such a column of dust does not have as much of a reddening effect as in the MW. This would indeed be solved by the make-up of the dust being different, but this is hard to explain given the well-determined extinction laws that are observed in GRB afterglows, which are consistent with the Local Group extinction laws (Schady et al. 2011; Greiner et al. 2011).

The reason for the scatter thus remains unclear, and we therefore advise significant caution against basing A_V predictions on the A_V to $N(H)$ ratio of the MW and Local Group. We also suggest that the discrepancy between the different methods of quantifying dust is the reason for the disagreement between the trend, or non-trend, seen in DTM with metallicity.

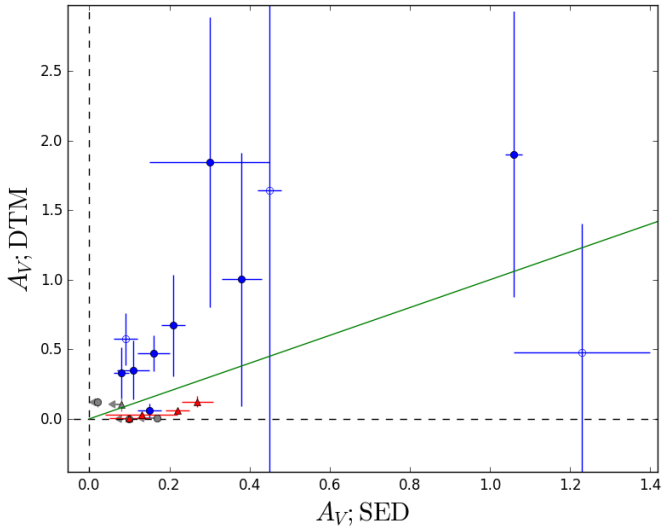


Fig. 8. A_V as measured directly from the SED against that calculated from the DTM. The green line indicates a 1:1 conversion between the two. Blue circles represent SEDs best fit with a simple power-law, whereas red triangles are used for broken power-law fits. Empty points refer to depletion measured from low-resolution spectra.

7. Conclusion

Gamma-ray bursts are a very useful, if not the best, probe of the dust-to-metals ratio in the high redshift Universe. We have used optical/NIR spectroscopy from a sample of 19 GRB afterglows in order to measure the metal and dust content of the DLAs in their host galaxies, including previously un-published metal column densities and metallicities for five objects. By using dust depletion models based on the MW as well as QSO-DLAs, we have used a thorough method to determine the column densities of dust and of metals, in order to calculate a dust-to-metals ratio. We find that the DTM follows a positive trend with metallicity, supporting the theory that a significant amount of dust is formed in-situ in the ISM. We investigated the discrepancy between the results of De Cia et al. (2013) and Zafar & Watson (2013), concluding that $A_{V;SED}$ and depletion are not analogous measurements of dust. We see the common trend that $A_{V;DTM}$ is often higher than $A_{V;SED}$, which we tentatively suggest could be due to the scaling between depletion-measured DTM and A_V being different in GRB host galaxies to the MW. We also notice a significant number of objects whose $A_{V;DTM}$ values are under predictions compared to $A_{V;SED}$, and despite seeing what looks like two distinct populations, are unable to satisfactorily reconcile the two using theories such as grey dust or intervening systems. We thus suggest that, given the large scatter between the two, DTM measured from depletion should not be used as a proxy for A_V , and encourage further work with larger samples to investigate the problem further.

Acknowledgements. We are grateful for the support of the GROND GRB team. We thank Annalisa De Cia, Darach Watson and Johan Fynbo for interesting and useful discussions. We thank C. Ledoux and P. Vreeswijk for providing a compilation of oscillator strengths. P.W and R.M.Y acknowledges support through the Sofja Kovalevskaja Award to P.S from the Alexander von Humboldt Foundation of Germany. Part of the funding for GROND (both hardware as well as personnel) was generously granted from the Leibniz-Prize to Prof. G. Hasinger (DFG grant HA 1850/28-1).

References

- Asplund, M., Grevesse, N., Sauval, A. J., & Scott, P. 2009, *Astrophys. Space Sci.*, 47, 481
- Bernstein, R. A., Freedman, W. L., & Madore, B. F. 2002, *Astrophys. J.*, 571, 56
- Bohlin, R. C., Savage, B. D., & Drake, J. F. 1978, *Astrophys. J.*, 224, 132
- Burrows, D. N., Hill, J. E., Nousek, J. a., et al. 2005, *Space Sci. Rev.*, 120, 165
- Chen, B., Dai, X., Kochanek, C. S., & Chartas, G. 2013, arXiv: 1306.0008 [arXiv:1306.0008]
- Cucchiara, A., Fumagalli, M., Rafelski, M., et al. 2015, *Astrophys. J.*, 804, 51
- De Cia, A., Ledoux, C., Mattsson, L., et al. 2016, *Astron. Astrophys.*, submitted
- De Cia, A., Ledoux, C., Savaglio, S., Schady, P., & Vreeswijk, P. M. 2013, *Astron. Astrophys.*, 560, A88
- D’Elia, V. 2010, *Astron. Astrophys.*, 523, A36
- D’Elia, V., Campana, S., Covino, S., et al. 2011, *Mon. Not. R. Astron. Soc.*, 418, 680
- D’Elia, V., Fynbo, J. P. U., Goldoni, P., et al. 2014, *Astron. Astrophys.*, 564, A38
- Draine, B. 2003, *Annu. Rev. Astron. Astrophys.*, 41, 241
- Draine, B. 2009, in *Cosm. Dust - Near Far*, ed. T. Henning, E. Grün, & J. Steinacker, Vol. 414, 453
- Dwek, E. 2016, arXiv: 1605.01957 [arXiv:1605.01957]
- Edmunds, M. G. & Eales, S. A. 1998, *Mon. Not. R. Astron. Soc.*, 299, L29
- Elíasdóttir, Á., Fynbo, J. P. U., Hjorth, J., et al. 2009, *Astrophys. J.*, 697, 1725
- Feldmann, R. 2015, *Mon. Not. R. Astron. Soc.*, 449, 3274
- Franco, J. & Cox, D. P. 1986, *Astron. Soc. Pacific*, 98, 1076
- Friis, M. 2015, Phd dissertation, University of Iceland, Reykjavík
- Friis, M., De Cia, A., Krühler, T., et al. 2015, *Mon. Not. R. Astron. Soc.*, 451, 167
- Fynbo, J. P. U., Ledoux, C., Noterdaeme, P., et al. 2011, *Mon. Not. R. Astron. Soc.*, 413, 2481
- Fynbo, J. P. U., Prochaska, J. X., Sommer-larsen, J., Dessauges-zavadsky, M., & Møller, P. 2008, *Astrophys. J.*, 683, 321
- Galama, T. J., Vreeswijk, P. M., van Paradijs, J., et al. 1998, *Nature*, 395, 670
- Gehrels, N., Chincarini, G., Giommi, P., et al. 2004, *Astrophys. J.*, 611, 1005
- Genzel, R., Lutz, D., Sturm, E., et al. 1998, *Astrophys. J.*, 498, 579
- Goldoni, P., Royer, F., François, P., et al. 2006, *Ground-based Airborne Instrum. Astron. Ed. by McLean*, 6269, 80
- Greiner, J., Kruehler, T., Fynbo, J. P. U., et al. 2008, eprint arXiv, 0810, 2314
- Greiner, J., Krühler, T., Klose, S., et al. 2011, *Astron. Astrophys.*, 526, A30
- Güver, T. & Özel, F. 2009, *Mon. Not. R. Astron. Soc.*, 400, 2050
- Issa, M. R., MacLaren, I., & Wolfendale, A. W. 1990, *Astron. Astrophys.*, 236, 237
- Jenkins, E. B. 2009, *Astrophys. J.*, 700, 1299
- Kann, D. A., Klose, S., Zhang, B., et al. 2010, *Astrophys. J.*, 720, 1513
- Krühler, T., Küpcü Yoldaş, A., Greiner, J., et al. 2008, *Astrophys. J.*, 685, 376
- Krühler, T., Ledoux, C., Fynbo, J. P. U., et al. 2013, *Astron. Astrophys.*, 557, A18
- Krühler, T., Malesani, D., Fynbo, J. P. U., et al. 2015, *Astron. Astrophys.*, 581, A125
- Ledoux, C., Vreeswijk, P. M., Smette, A., et al. 2009, *Astron. Astrophys.*, 506, 661
- Mannucci, F., Salvaterra, R., & Campisi, M. A. 2011, *Mon. Not. R. Astron. Soc.*, 414, 1263
- Mattsson, L. 2016 [arXiv:1606.02272]
- Mattsson, L., De Cia, A., Andersen, A. C., & Zafar, T. 2014, *Mon. Not. R. Astron. Soc.*, 440, 1562
- McKee, C. C. F. & Ostriker, E. C. E. 2007, *Annu. Rev. Astron. Astrophys.*, 45, 565
- McKinnon, R., Torrey, P., & Vogelsberger, M. 2016, *Mon. Not. R. Astron. Soc.*, 457, 3775
- Meszáros, P. & Rees, M. J. 1997, *Astrophys. J.*, 476, 232
- Modigliani, A., Goldoni, P., Royer, F., et al. 2010, *Obs. Oper. Strateg.*, 7737, 56
- Peeters, E., Spoon, H. W. W., & Tielens, A. G. G. M. 2004, *Astrophys. J.*, 613, 986
- Pei, Y. C. 1992, *Astrophys. J.*, 395, 130
- Predehl, P. & Schmitt, J. H. M. M. 1995, *Astron. Astrophys.*, 293, 889
- Prochaska, J. X., Chen, H.-W., Dessauges-Zavadsky, M., & Bloom, J. S. 2007, *Astrophys. J.*, 666, 267
- Rau, A., Savaglio, S., Krühler, T., et al. 2010, *Astrophys. J.*, 720, 862
- Sanders, D. B. & Mirabel, I. F. 1996, *Annu. Rev. Astron. Astrophys.*, 34, 749
- Savage, B. D. B. & Sembach, K. R. K. 1996, *Annu. Rev. Astron. Astrophys.*, 34, 279
- Savaglio, S. 2001, in *Extragalactic Infrared Backgr. its Cosmol. Implic. IAU Symp.*, Vol. 204, 307
- Savaglio, S., Fall, S. M., & Fiore, F. 2003, *Astrophys. J.*, 585, 638
- Savaglio, S., Glazebrook, K., & Le Borgne, D. 2009, *Astrophys. J.*, 691, 182
- Savaglio, S., Rau, A., Greiner, J., et al. 2012, *Mon. Not. R. Astron. Soc.*, 420, 627
- Schady, P., Dwelly, T., Page, M. J., et al. 2012, *Astron. Astrophys.*, 536, A15

- Schady, P., Page, M. J., Oates, S. R., et al. 2010, *Mon. Not. R. Astron. Soc.*, 401, 2773
- Schady, P., Savaglio, S., Krühler, T., Greiner, J., & Rau, A. 2011, *Astron. Astrophys.*, 525, 1
- Schlafly, E. F. & Finkbeiner, D. P. 2011, *Astrophys. J.*, 737, 103
- Skúladóttir, Á. 2010, Master thesis, Univ. Copenhagen
- Smette, A., Sana, H., Noll, S., et al. 2015, *Astron. Astrophys.*, 576, A77
- Sparre, M., Hartoog, O. E., Krühler, T., et al. 2014, *Astrophys. J.*, 785, 150
- Starling, R. L. C., Wijers, R. a. M. J., Wiersema, K., et al. 2007, *Astrophys. J.*, 661, 787
- Tanvir, N. R., Fox, D. B., Levan, a. J., et al. 2009, *Nature*, 461, 1254
- Tchernyshyov, K., Meixner, M., Seale, J., et al. 2015, *Astrophys. J.*, 811, 78
- Thöne, C. C., Fynbo, J. P. U., Goldoni, P., et al. 2013, *Mon. Not. R. Astron. Soc.*, 428, 3590
- Vladilo, G. 2004, *Astron. Astrophys.*, 421, 479
- Vladilo, G., Abate, C., Yin, J., Cescutti, G., & Matteucci, F. 2011, *Astron. Astrophys.*, 530, A33
- Watson, D. 2011, *Astron. Astrophys.*, 533, A16
- Watson, D. J., Fynbo, J. P. U., Ledoux, C., et al. 2006, *Astrophys. J.*, 652, 1011
- Wolfe, A. M., Gawiser, E., & Prochaska, J. X. 2005, *Annu. Rev. Astron. Astrophys.*, 43, 861
- Zafar, T. & Watson, D. 2013, *Astron. Astrophys.*, 560, A26

Appendix A:

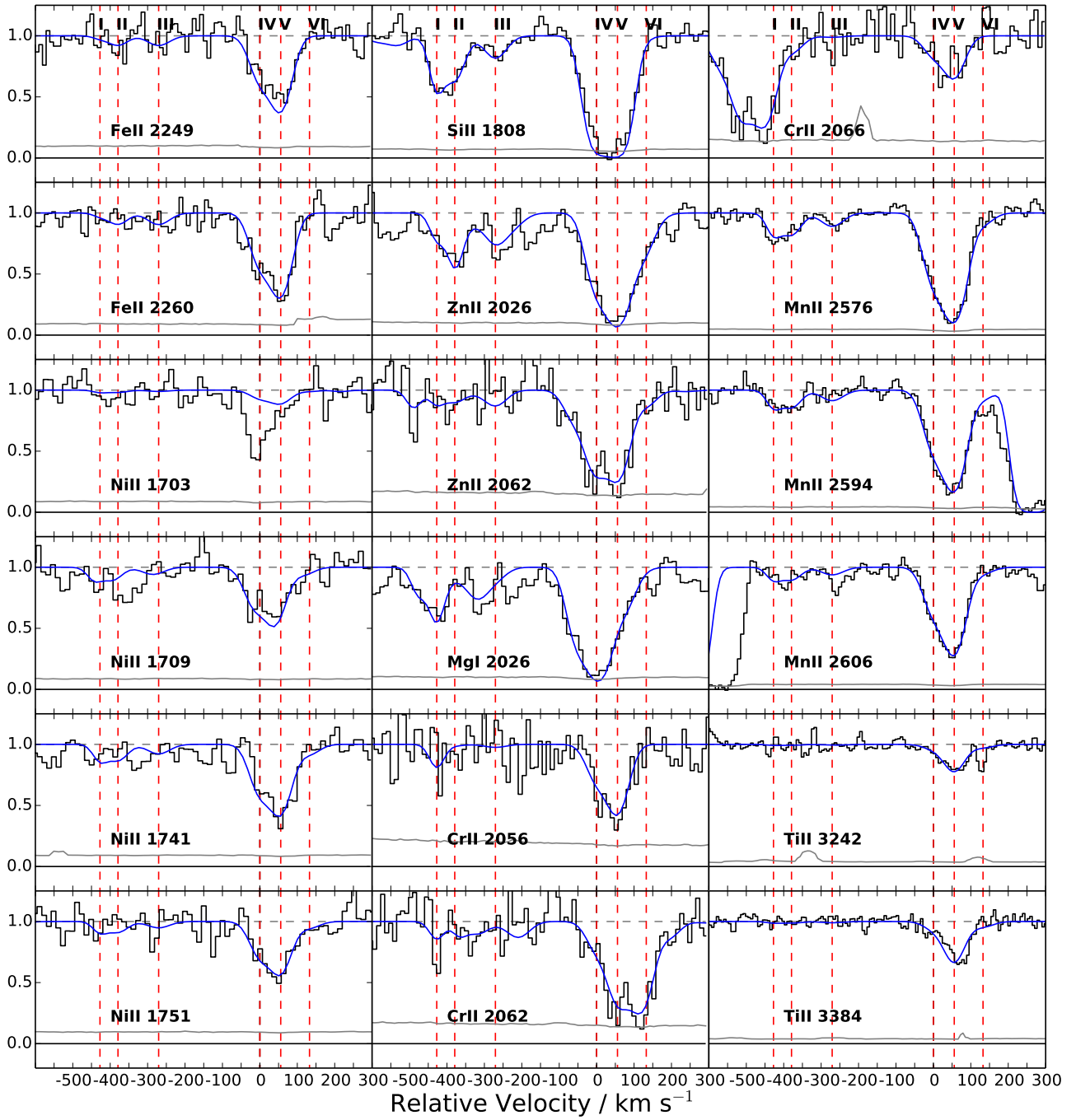


Fig. A.1. Metal absorption lines in the X-Shooter spectrum of GRB 120119A. Resolution in VIS arm: $v = 31.4 \text{ km s}^{-1}$.

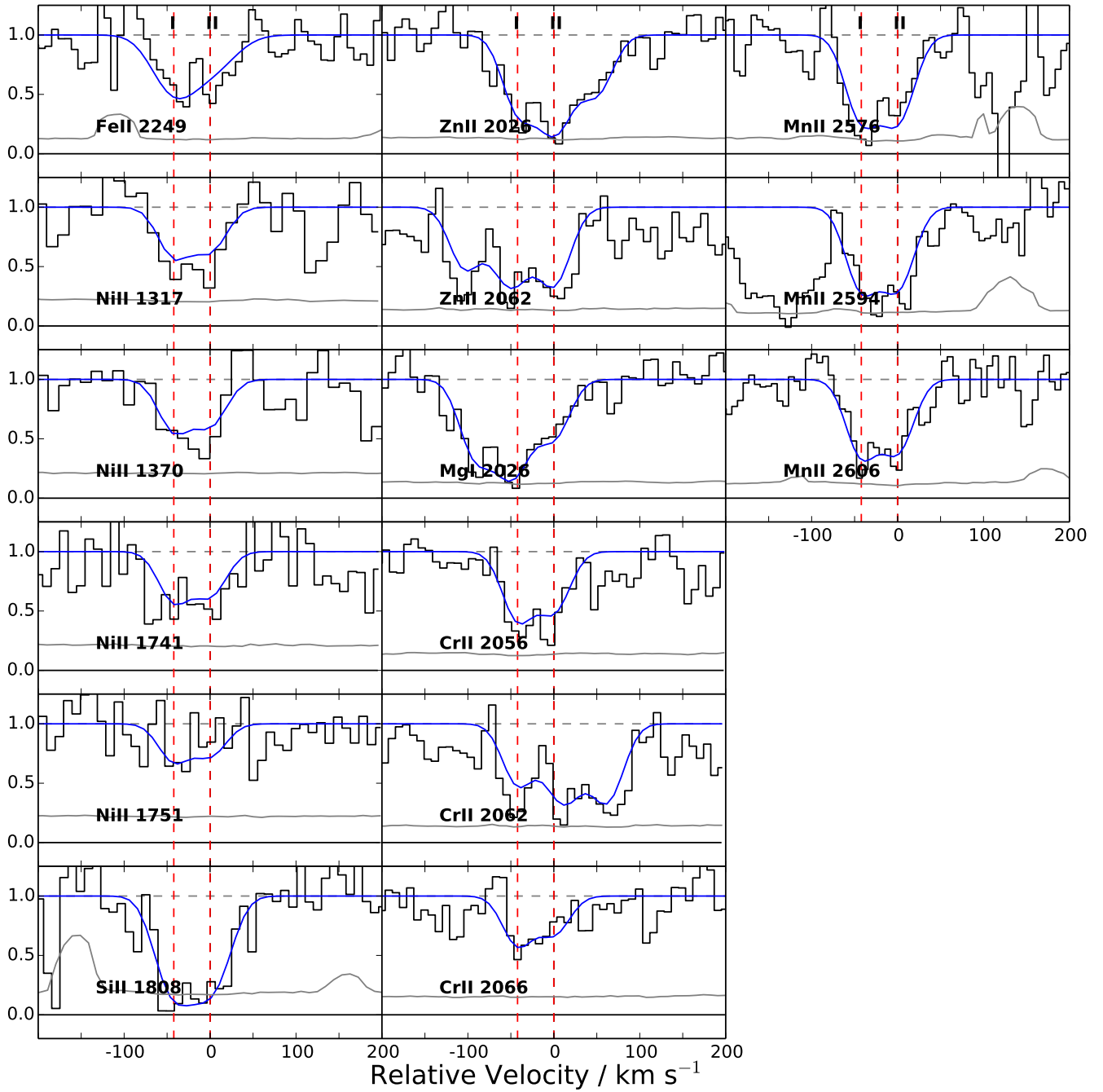


Fig. A.2. Metal absorption lines in the X-Shooter spectrum of GRB 120716A. Resolution in VIS arm: $v = 35.0 \text{ km s}^{-1}$.

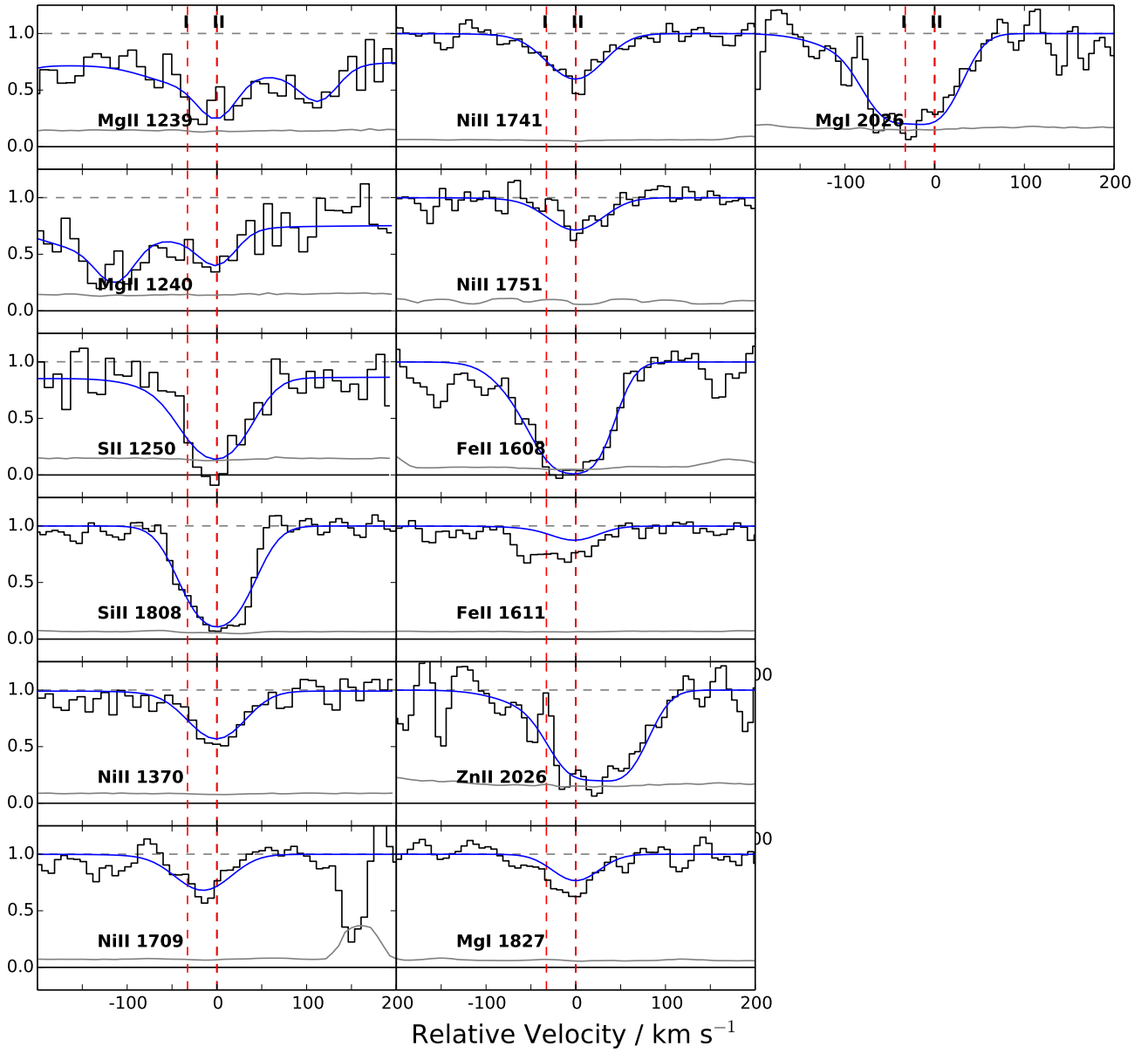


Fig. A.3. Metal absorption lines in the X-Shooter spectrum of GRB 120909A. Resolution in VIS arm: $v = 30.1 \text{ km s}^{-1}$. The extra absorption apparent in Fe II 1611 is from the excited state transition Fe II 5s 1612.

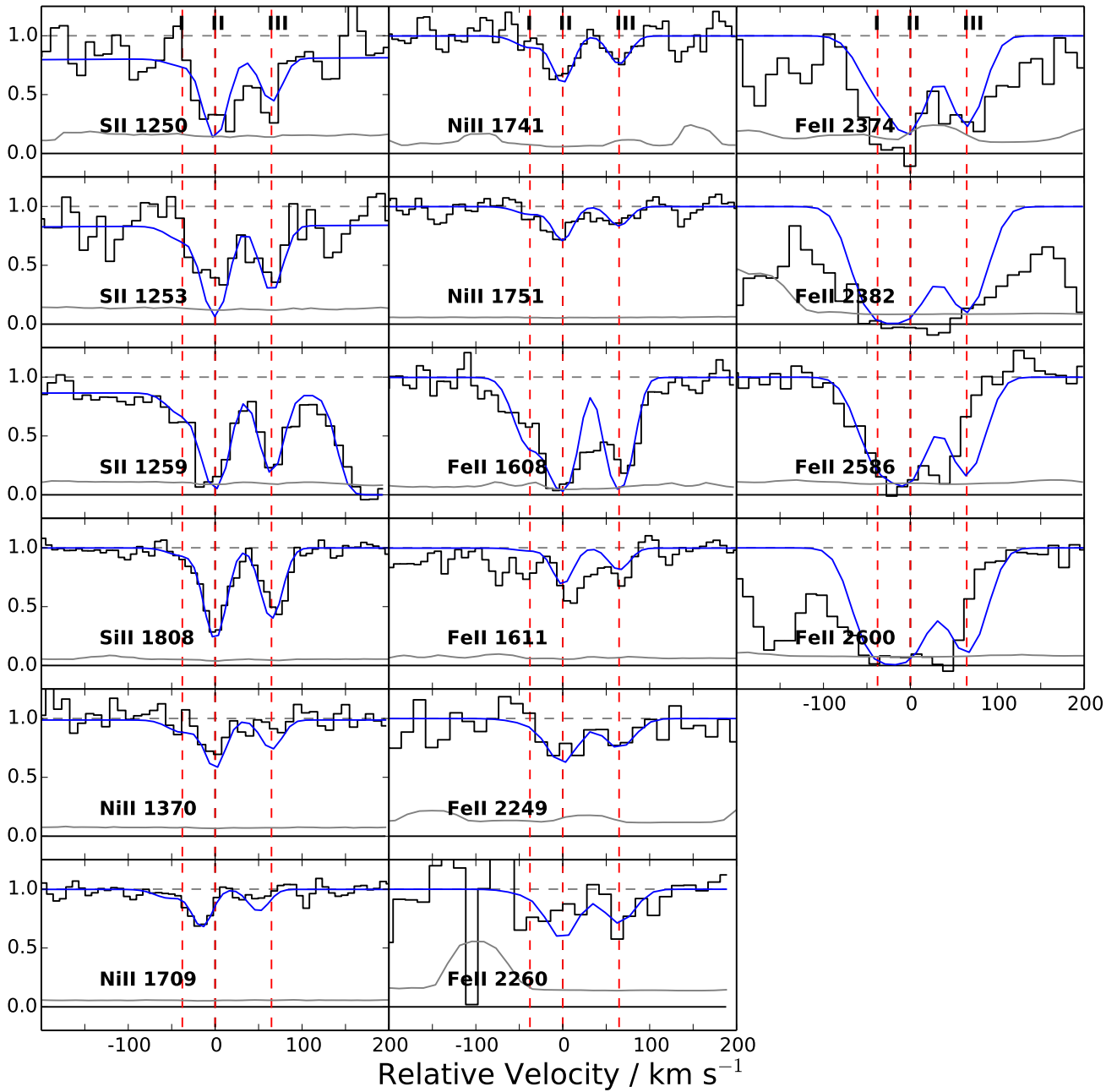


Fig. A.4. Metal absorption lines in the X-Shooter spectrum of GRB 130408A. Resolution in VIS arm: $v = 20.0 \text{ km s}^{-1}$.

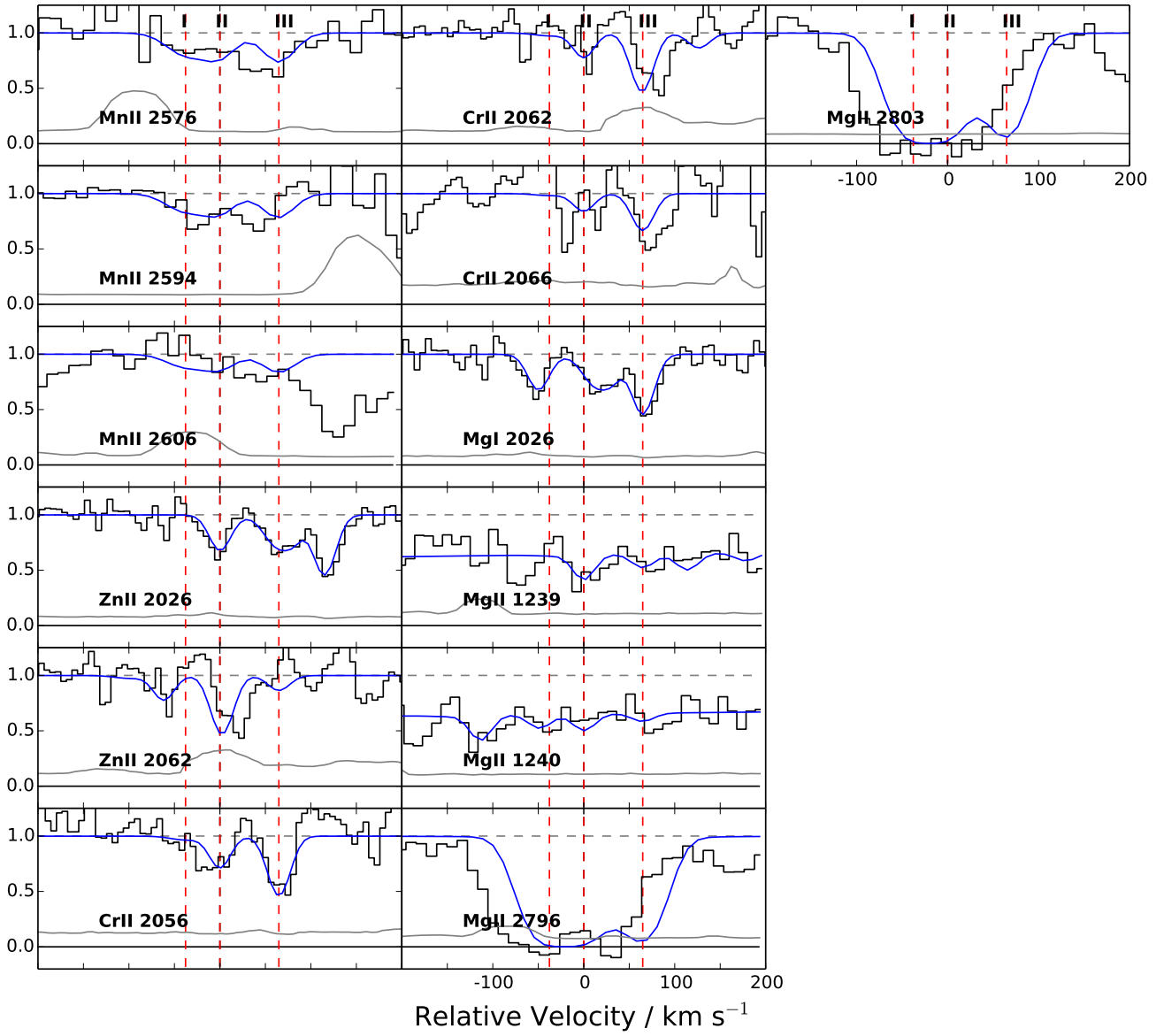


Fig. A.5. Metal absorption lines in the X-Shooter spectrum of GRB 130408A. Resolution in VIS arm: $v = 20.0 \text{ km s}^{-1}$.

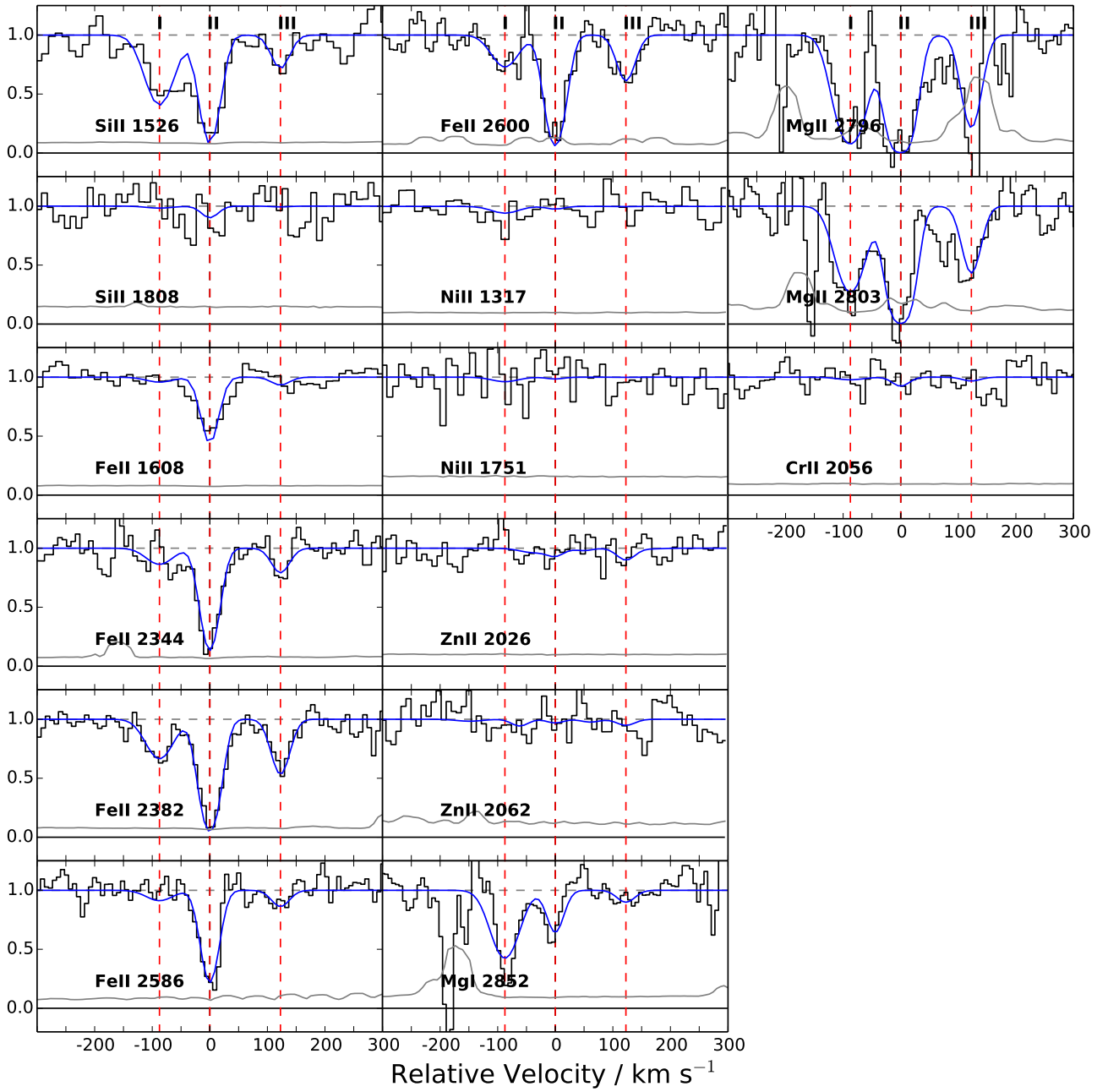


Fig. A.6. Metal absorption lines in the X-Shooter spectrum of GRB 141028A. Resolution in VIS arm: $v = 25.0 \text{ km s}^{-1}$.

Appendix B:

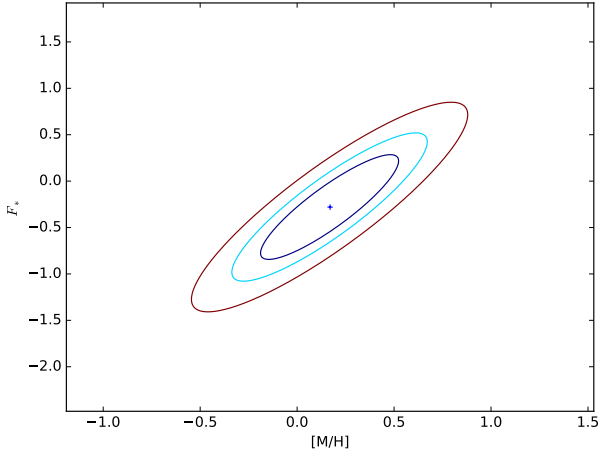


Fig. B.1. Confidence regions for F_* and $[M/H]$ for GRB 000926.

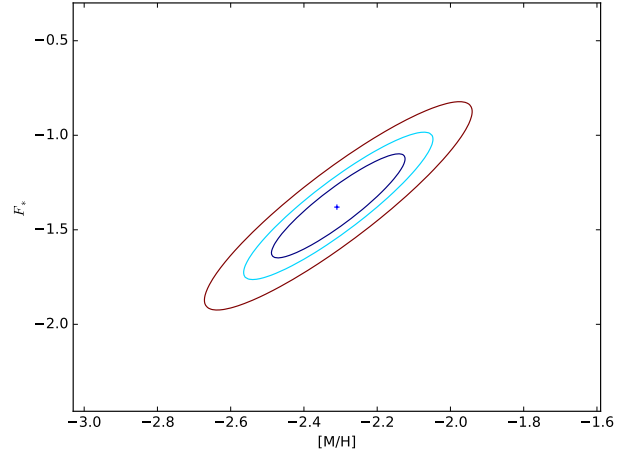


Fig. B.3. Confidence regions for F_* and $[M/H]$ for GRB 050730.

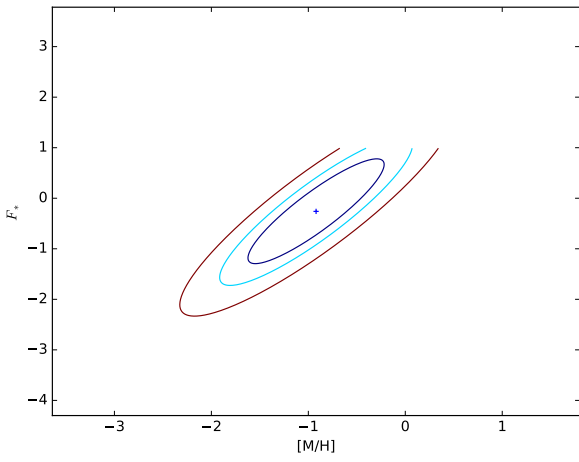


Fig. B.2. Confidence regions for F_* and $[M/H]$ for GRB 050401.

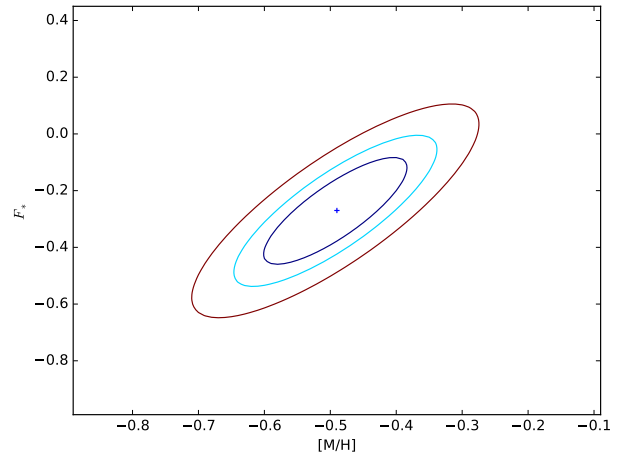


Fig. B.4. Confidence regions for F_* and $[M/H]$ for GRB 050820A.

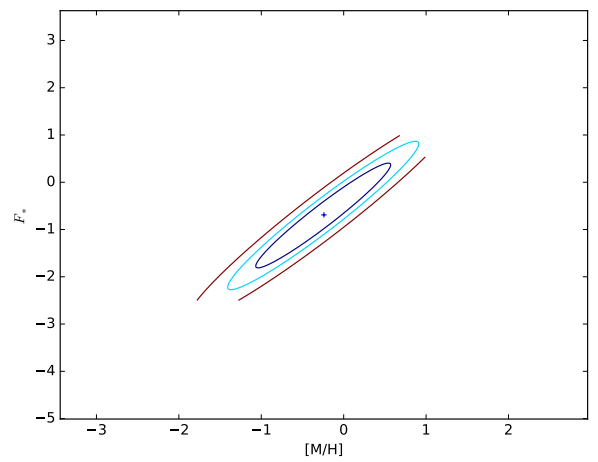


Fig. B.5. Confidence regions for F_* and $[M/H]$ for GRB 070802.

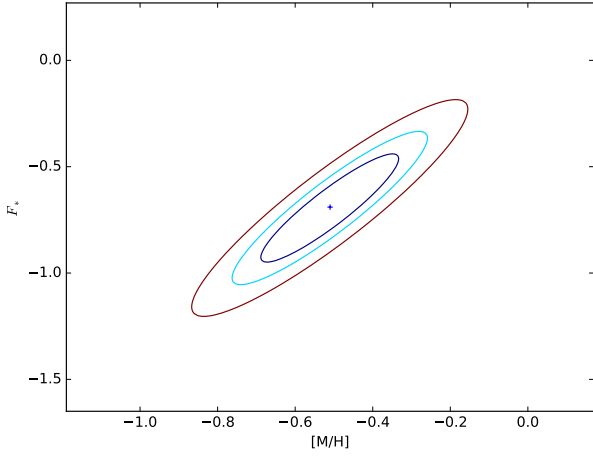


Fig. B.6. Confidence regions for F_* and $[M/H]$ for GRB 081008.

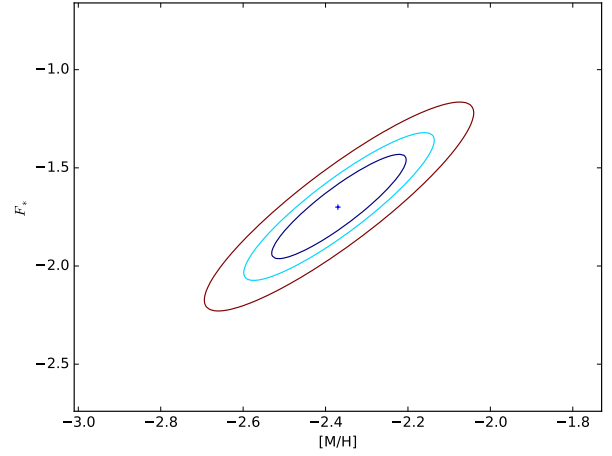


Fig. B.9. Confidence regions for F_* and $[M/H]$ for GRB 090926A.

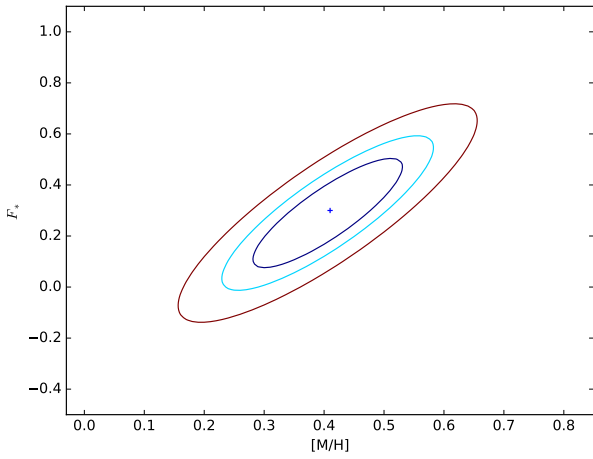


Fig. B.7. Confidence regions for F_* and $[M/H]$ for GRB 090323.

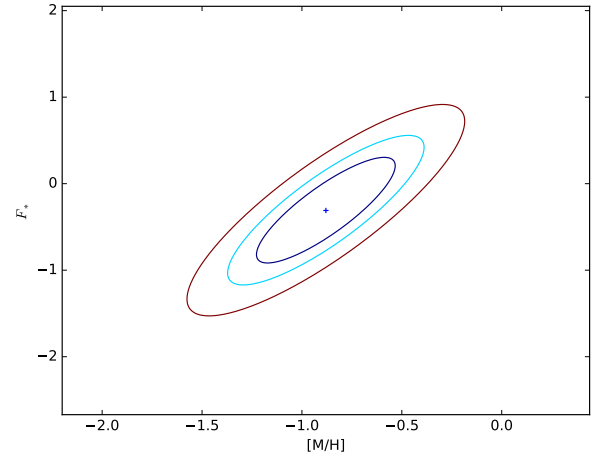


Fig. B.10. Confidence regions for F_* and $[M/H]$ for GRB 100219A.

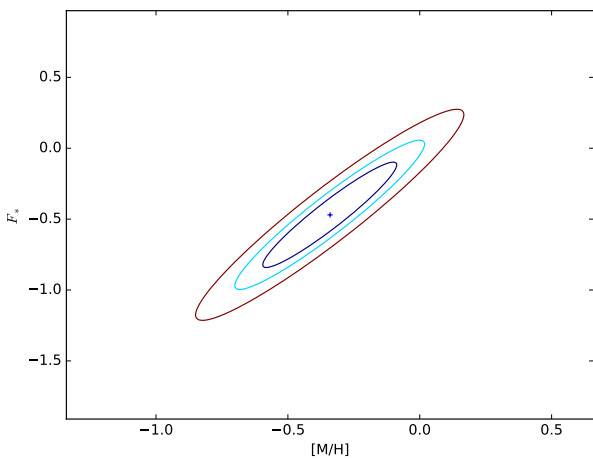


Fig. B.8. Confidence regions for F_* and $[M/H]$ for GRB 090809F.

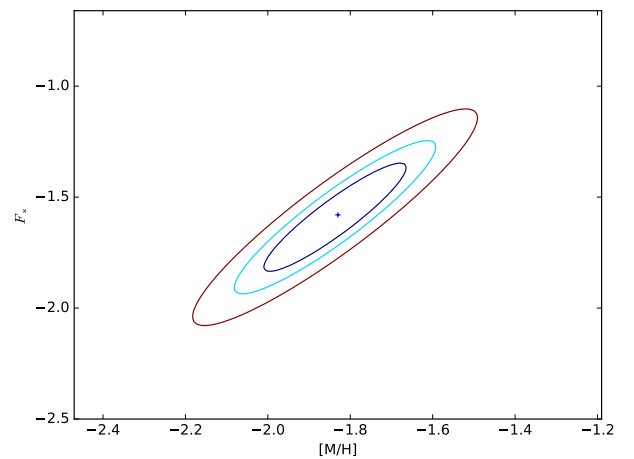


Fig. B.11. Confidence regions for F_* and $[M/H]$ for GRB 111008A.

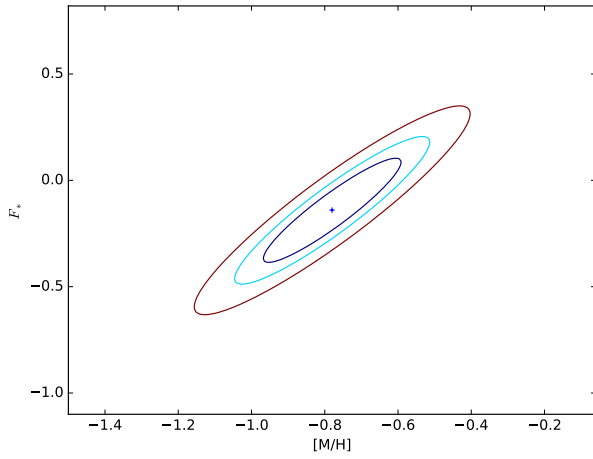


Fig. B.12. Confidence regions for F_* and $[M/H]$ for GRB 120119A.

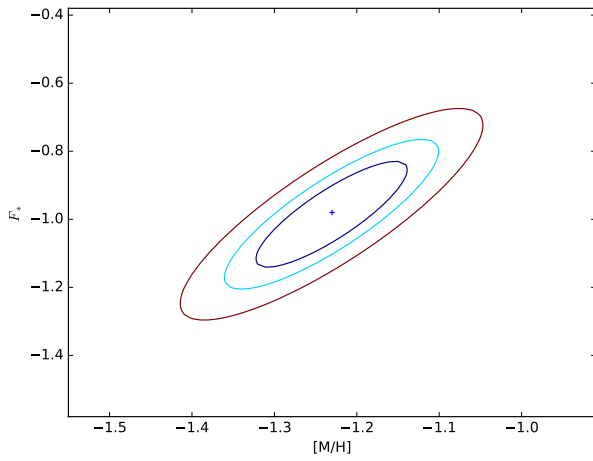


Fig. B.13. Confidence regions for F_* and $[M/H]$ for GRB 120327A.

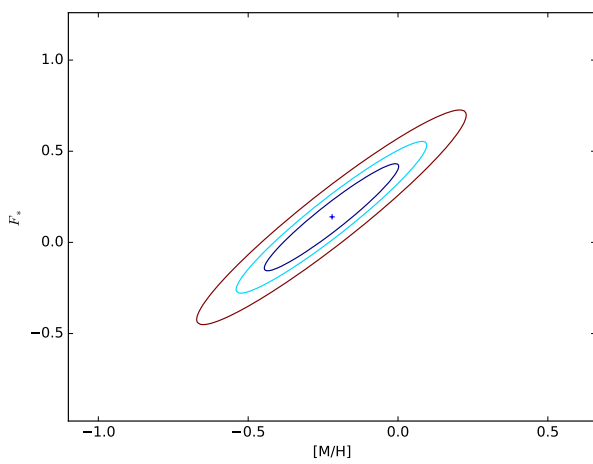


Fig. B.14. Confidence regions for F_* and $[M/H]$ for GRB 120716A.

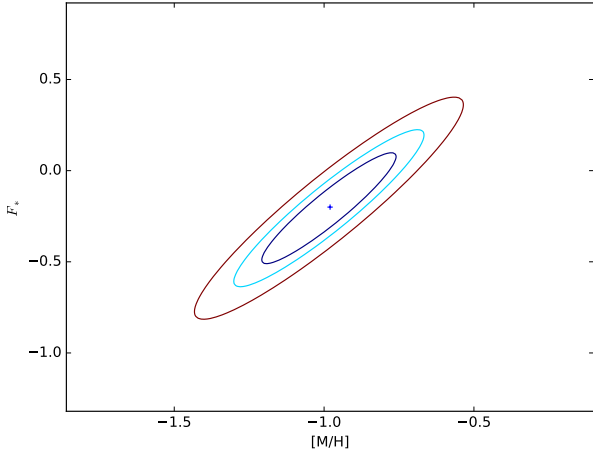


Fig. B.15. Confidence regions for F_* and $[M/H]$ for GRB 120815A.

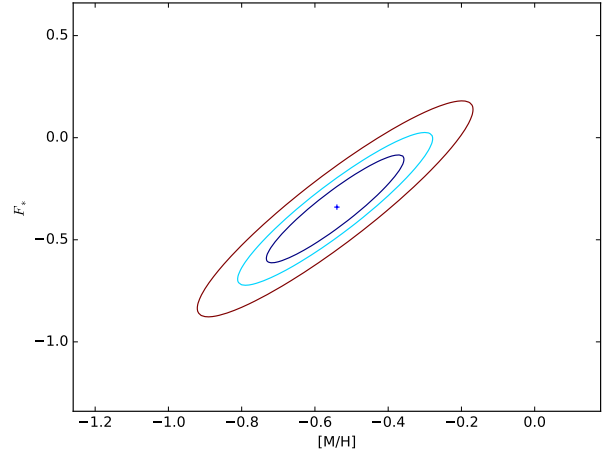


Fig. B.17. Confidence regions for F_* and $[M/H]$ for GRB 121024A.

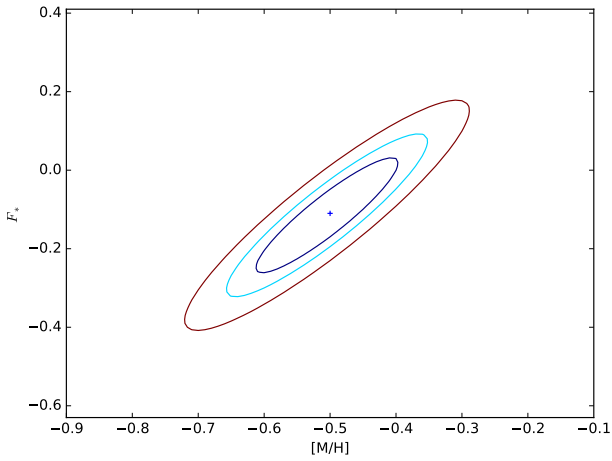


Fig. B.16. Confidence regions for F_* and $[M/H]$ for GRB 120909A.

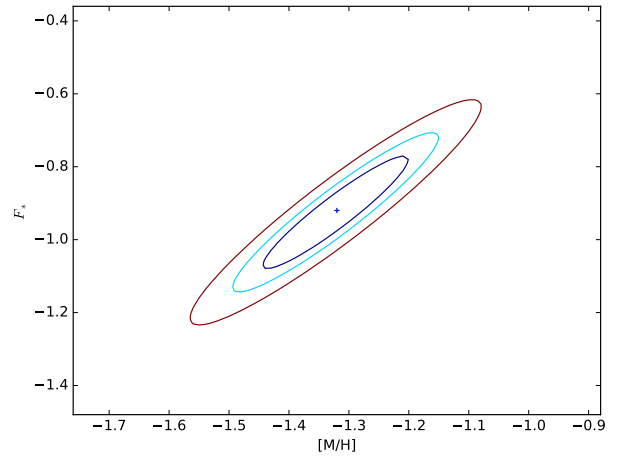


Fig. B.18. Confidence regions for F_* and $[M/H]$ for GRB 130408A.

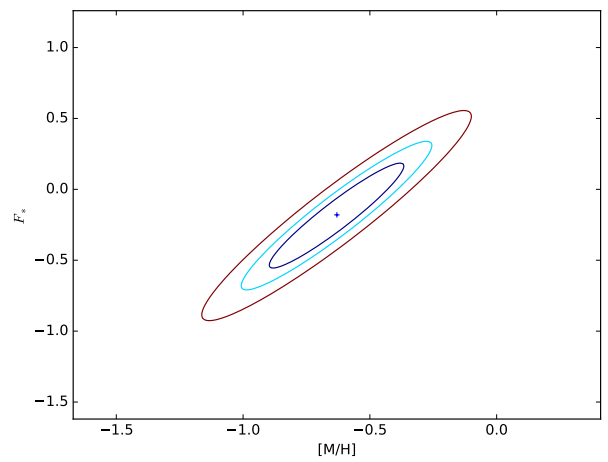


Fig. B.19. Confidence regions for F_* and $[M/H]$ for GRB 141028A.